

International Journal of Modern Physics A
© World Scientific Publishing Company

Neutrino Dipole Portal

Sin Kyu Kang

*School of Natural Science, Seoul National University of Science Technology, Gongreung-ro 232
Seoul, 01811, Republic of Korea
skkang@seoultech.ac.kr*

C.J. Ouseph

*Institute of Convergence Fundamental Studies, Seoul National University of Science and
Technology, Seoul 01811, Korea*

Received Day Month Year
Revised Day Month Year

The neutrino dipole portal (NDP) is a minimal and predictive extension of the Standard Model, in which a transition magnetic moment operator couples an active neutrino to a heavy neutral lepton via the electromagnetic field. This higher-dimensional interaction gives rise to distinctive processes such as neutrino up-scattering, radiative decays, meson transitions, and modifications of recoil spectra, offering multiple avenues for discovery. In this review, we discuss the theoretical foundations of the NDP, its ultraviolet completions, and the associated production and decay mechanisms across laboratory, astrophysical, and cosmological settings. Current constraints arise from accelerator searches, recoil-based detectors, collider studies, and high energy neutrino observatories, complemented by robust bounds from Big Bang Nucleosynthesis, the Cosmic Microwave Background, and supernova cooling. Future experimental and observational efforts, including next-generation neutrino experiments, multi-ton dark matter detectors, and improved cosmological and astrophysical probes, are anticipated to test the remaining allowed regions. The NDP thus provides a simple, well-motivated, and broadly testable framework at the intersection of particle physics, astrophysics, and cosmology.

Keywords: Neutrino Dipole Portal; Heavy Neutral Lepton; Neutrino Scattering Experiments; Astrophysics Constraints

1. Introduction

Neutrino oscillation experiments^{1–3} provided unambiguous evidence for nonzero neutrino masses, a finding fundamentally incompatible with the Standard Model (SM), which admits only massless neutrinos. This breakthrough transformed our view of fundamental interactions and motivated intensive theoretical and experimental research aimed at elucidating the origin of neutrino masses and their significance for physics beyond the SM. A variety of mechanisms have been proposed to account for the smallness of neutrino masses, including canonical seesaw mechanisms,^{4,7,8} radiative generation models,^{9,10} and extra-dimensional frameworks.^{11,12} Despite impressive experimental progress, the precise mechanism remains elusive.

Among the many theoretical candidates, sterile neutrinos occupy a prominent place.^{13–15} Sterile neutrinos are electroweak singlets, insensitive to SM gauge interactions but potentially mixing with active neutrinos. They arise naturally in seesaw frameworks, where their inclusion can elegantly explain the lightness of active neutrino masses, and they frequently appear in models connecting the visible and hidden (dark) sectors.^{16–18} Their masses are essentially free parameters, spanning from the sub-eV scale to the Planck scale, although scenarios tied to neutrino mass generation often restrict them below the TeV scale. Because of this versatility, sterile neutrinos serve as natural extensions of the SM and as a bridge between laboratory anomalies, cosmological observations, and astrophysical phenomena.^{14, 19}

Another important aspect of neutrino physics concerns their electromagnetic (EM) properties.^{20–22} In the SM, neutrinos are electrically neutral and possess only tiny magnetic moments, generated radiatively at higher order.^{22–24} For Dirac neutrinos, the expected value is of order $\mu_\nu^{\text{SM}} \sim 10^{-19}(m_\nu/1\text{eV})\mu_B$, far below current experimental sensitivity.^{25, 26} Historically, the idea of neutrino magnetic moments played a central role: Schwinger first speculated on their existence,²⁷ Cisneros proposed them as a possible resolution of the solar neutrino problem,²⁸ and many experiments have pursued them as clean signals of new physics.

Beyond the SM, a wide range of theories can generate substantially larger magnetic or transition dipole moments.²⁹ In particular, if sterile neutrinos or heavy neutral leptons (HNLs) exist in the keV–GeV mass range, they can mix with active neutrinos and acquire transition dipole moments large enough to be observable. This possibility opens new avenues for discovery, allowing neutrinos to engage in EM interactions such as radiative decays or photon mediated scattering. Such processes are highly distinctive experimentally, often leading to clean single-photon signatures or distortions of recoil spectra at low energies.

A natural framework for describing these interactions is the *Neutrino Dipole Portal* (NDP). The NDP is an effective field theory (EFT) extension in which a dimension-five operator couples an active neutrino to a HNL through the EM field tensor,

$$\mathcal{L}_{\text{NDP}} \supset \mu_{\nu N} \bar{\nu}_L \sigma^{\mu\nu} N_R F_{\mu\nu},$$

where $\mu_{\nu N}$ denotes the transition dipole moment. Hereafter, we denote $N \equiv N_R$ for simplicity and use the term "HNL" in place of sterile neutrino. This operator is chirality-flipping, gauge-invariant, and can be UV-completed in multiple ways, often involving heavy charged fermions or scalars in loops.^{30, 31} Its theoretical appeal lies in its minimality, as the entire phenomenology is governed by a single parameter $\mu_{\nu N}$, and in its robustness, since dipole operators naturally appear in effective Lagrangian once heavy fields are integrated out.

The phenomenology of the NDP is exceptionally rich, encompassing processes such as neutrino up-scattering ($\nu A \rightarrow N A$, $\nu e \rightarrow N e$), radiative decays ($N \rightarrow \nu\gamma$), and Dalitz-like meson decays ($\pi^0 \rightarrow \gamma\nu N$). It also gives rise to displaced photon vertices, delayed photon signatures, and modifications of elastic recoil spectra.

Recent theoretical and phenomenological studies^{32–34} have emphasized several distinctive features: (i) the NDP produces cross sections enhanced at low recoil energies, scaling approximately as $1/E$, which gives experiments with low thresholds a significant advantage; (ii) the operator mediates radiative decays, so displaced or delayed photon signals arise naturally and serve as smoking-gun signatures; and (iii) in gauge-invariant completions the operator is embedded in higher-dimensional structures, ensuring theoretical consistency and linking dipole portal phenomenology with broader classes of models. These phenomena can be tested across an exceptionally wide range of environments, including accelerator-based neutrino experiments, colliders, reactor and solar neutrino facilities, dark matter detectors, astrophysical systems such as supernovae, and cosmology through Big Bang Nucleosynthesis (BBN) and the Cosmic Microwave Background (CMB). The fact that the same operator connects such disparate frontiers makes the NDP a powerful unifying framework for new physics searches. NDP scenarios have even been invoked to explain anomalies such as the MiniBooNE low-energy excess,³⁵ although such interpretations are now tightly constrained by complementary data.

Experimentally, a diverse program of searches constrains the NDP interactions. Laboratory experiments have already reached impressive sensitivities: CE ν NS measurements from COHERENT,³⁶ electron recoil experiments such as Borexino³⁷ and TEXONO,³⁸ and dark matter detectors like XENONnT³⁹ and PandaX⁴⁰ probe down to $\mu_{\nu N} \sim 10^{-10} \mu_B$. Astrophysical and cosmological constraints are even stronger: arguments from SN1987A cooling,⁴² modifications to BBN,⁴³ and CMB determinations of N_{eff}^{44} reach $\mu_{\nu N} \lesssim 10^{-11} \mu_B$. These bounds are highly robust, being largely free of detector systematics, though they are subject to astrophysical uncertainties. Laboratory, astrophysical, and cosmological probes already exclude wide regions of parameter space, while leaving open motivated windows that can be tested in the near future.

In this review, we present a systematic exploration of the NDP. Our aim is to integrate its theoretical foundations with its phenomenological implications, providing a coherent picture across energy, intensity, astrophysical, and cosmological frontiers. The structure of the paper is as follows. In Sec. 2, we introduce the NDP operator, discuss its Lorentz and gauge structure, review possible ultraviolet completions, and summarize its main phenomenological consequences. In Sec. 3, we examine sterile neutrino production through the dipole portal, presenting analytic expressions for cross sections and decay widths and highlighting how the operator modifies neutrino processes across up-scattering, dipole-induced meson decays, and collider channels. In Sec. 4, we classify and review experimental search strategies, including fixed-target facilities, colliders, and recoil-based low-threshold detectors. Section 5 presents a unified overview of present bounds and projected sensitivities on the NDP from laboratory, astrophysical, and cosmological probes. Finally, in Sec. 6, we summarize the state of the field, highlight the complementarity of existing probes, and outline promising directions for future searches. Some useful

formulae are provided in the Appendix.

2. Theoretical Framework

At low energies, the NDP is described by the dimension-five operator^{30,33,34}

$$\mathcal{L}_{\text{NDP}} = \frac{\mu_{\nu N}}{2} \bar{\nu} \sigma^{\mu\nu} N F_{\mu\nu} + \text{h.c.}, \quad (1)$$

where ν denotes an active neutrino, N is a sterile gauge singlet, and $F_{\mu\nu} = \partial_\mu A_\nu - \partial_\nu A_\mu$ is the EM field strength tensor. The coefficient $\mu_{\nu N}$ has mass dimension -1 and is usually expressed in units of the Bohr magneton, $\mu_B = e/(2m_e)$, in order to facilitate comparison with neutrino magnetic moment searches. The bilinear $\bar{\nu} \sigma^{\mu\nu} N$ flips chirality, linking left-handed SM neutrinos to right-handed sterile states.

Neutrino magnetic moments were first discussed in the late 1970s and early 1980s,^{45–47} originally as possible explanations for solar neutrino anomalies.²⁸ In the SM extended with massive neutrinos, such moments arise radiatively but are extremely suppressed,^{24,26,48}

$$\mu_\nu^{\text{SM}} \simeq 3 \times 10^{-19} \left(\frac{m_\nu}{1 \text{ eV}} \right) \mu_B, \quad (2)$$

many orders of magnitude below experimental reach. This motivates studying extensions such as the NDP, where transition dipoles $\mu_{\nu N}$ can be much larger, naturally arising in ultraviolet (UV) completions with new charged fermions or scalars in loops.^{30,31} Importantly, in the limit $m_\nu \rightarrow 0$ an enhanced chiral symmetry is restored, ensuring that large transition dipoles do not destabilize the smallness of neutrino masses, in accordance with 't Hooft naturalness.³¹

In the SM effective field theory (SMEFT) extended with sterile fermions, the NDP arises from the higher-dimensional operator^{30,33}

$$\frac{c}{\Lambda^2} (\bar{L} \sigma^{\mu\nu} N) \tilde{H} B_{\mu\nu}, \quad (3)$$

where L is the lepton doublet, \tilde{H} is the conjugate Higgs, $B_{\mu\nu}$ is the hypercharge field strength, and Λ is the heavy scale. After electroweak symmetry breaking, this reduces to Eq. (1) with $\mu_{\nu N} \simeq c v/\Lambda^2$. The SMEFT embedding clarifies the gauge-invariant origin of the operator and its behavior under lepton number. For Dirac sterile fermions with $L(N) = 1$, the dipole interaction conserves lepton number, $\Delta L = 0$. For Majorana sterile states, only transition dipoles are allowed, while diagonal dipoles vanish identically.^{47,48}

In this review, we restrict attention to transition dipoles between active and sterile states of the form $\bar{\nu} \sigma_{\mu\nu} N F^{\mu\nu}$. We do not consider sterile–sterile dipole operators ($\bar{N} \sigma_{\mu\nu} N F^{\mu\nu}$). For Majorana N , such diagonal dipoles are forbidden, while for Dirac N they couple only sterile states to photons and do not induce active–sterile transitions. Although such terms could in principle induce small effective dipoles for active neutrinos in the presence of active–sterile mass mixing,^{49,50} we do not include this possibility here, since our focus is on the minimal dipole portal without mixing effects.

At the loop level, transition dipoles can be generated with a parametric size

$$\mu_{\nu N} \sim \frac{e}{16\pi^2} \frac{m}{M^2}, \quad (4)$$

where m denotes a chirality-flip mass insertion and M the heavy mass of the loop particle. Explicit UV completions include models with vector-like leptons or leptoquarks,^{30,31,51} where sizable $\mu_{\nu N}$ can be obtained while neutrino masses remain small. Such frameworks demonstrate that large dipoles can be realized consistently without destabilizing neutrino masses. In these cases the dipole portal may even dominate over mixing-mediated interactions, which are suppressed by small Dirac couplings or helicity suppression.^{31,34}

The NDP also opens a variety of new processes of phenomenological interest:

- *Radiative decay*: $N \rightarrow \nu\gamma$, with width $\Gamma \propto |\mu_{\nu N}|^2 M_N^3$ where M_N is a mass of HNL, often dominating over weak or mixing-induced decays for small active-sterile mixing.^{46,47}
- *Neutrino up-scattering*: $\nu + \mathcal{A} \rightarrow N + \mathcal{A}$, where \mathcal{A} can be a nucleus, proton, or electron. Cross sections receive coherent Z^2 enhancement for nuclear targets, making this process a powerful source of HNLs in beam-dump, reactor, and fixed-target experiments^{32,34,52}
- *Collider production*: $e^+e^- \rightarrow \nu N(\gamma)$ or $\gamma q \rightarrow Nq$, with signatures of displaced or prompt photons plus missing energy.^{53,54}
- *Recoil spectra*: Additional dipole channels modify ν - e elastic scattering (NEES) and coherent elastic neutrino-nucleus scattering (CE ν NS). These do not produce N directly but distort recoil distributions relative to the SM, leading to characteristic $1/E_T$ enhancements at low recoil energies.^{33,48,55,56}
- *Astrophysical and cosmological probes*: Enhanced plasmon decay rates, stellar cooling, supernova neutrino transport, and BBN constraints provide complementary sensitivity to the dipole moments.^{33,57,58}

The resulting signatures highlight the potential of the NDP to reveal new physics well beyond the SM through complementary experimental and observational probes.

3. Production Mechanisms

3.1. *Neutrino Up-scattering via the Dipole Portal*

Among the key production mechanisms for HNLs in the context of the NDP, *neutrino up-scattering* stands out as both distinctive and experimentally accessible.^{34,52} In this process, an incoming SM neutrino ν converts into a heavier state N through the dipole operator with coupling $\mu_{\nu N}$, mediated by the exchange of a virtual photon. The generic form of the reaction is

$$\nu(p) + \mathcal{A}(k) \rightarrow N(p') + \mathcal{A}(k'), \quad (5)$$

where \mathcal{A} denotes the target, which may be a nucleus, proton, or electron. The momentum transfer is characterized by $t = (p - p')^2$, and the dynamics are governed by the effective dipole interaction.

The neutrino up-scattering is especially relevant at the intensity frontier, such as beam-dump facilities and near-detector experiments, where intense neutrino fluxes interact with dense targets. The production probability increases with higher incoming neutrino energy E_ν and with larger HNL mass M_N (as long as kinematics permit), since the available phase space expands. This makes the neutrino up-scattering a powerful probe of the NDP across a broad range of energies and masses.

The scattering dynamics depend on the target composition and the momentum transfer, which broadly divides the interaction into two regimes:

- **Coherent scattering:** At low momentum transfer $|t|$, neutrinos scatter coherently off the entire nucleus and, at very low energies, even off the atomic electron cloud. For a nucleus with atomic number Z (protons) and neutron number N , the cross section acquires a coherence enhancement proportional to the square of the net charge distribution: approximately N^2 for neutral-current weak interactions, or Z^2 for purely EM interactions. This enhancement is reduced at higher $|t|$ by nuclear form factors.^{59–61} Coherent scattering dominates at low neutrino energies (tens of MeV) and small scattering angles.
- **Incoherent scattering:** At higher E_ν or larger $|t|$, the neutrino resolves individual nucleons or electrons. In this regime, the cross section scales only linearly with the number of scattering centers ($\propto Z$ for protons or electrons, $\propto A$ (mass number) for all nucleons), lacking the collective A^2 or N^2 coherence enhancement. Incoherent scattering becomes dominant once nucleon recoil or nuclear breakup is kinematically accessible.^{61, 62}

The target type determines which regime dominates in practice:

- **Nuclear targets** support both coherent and incoherent interactions. At low momentum transfer, coherence leads to an enhancement scaling as $\sim N^2$ for neutral-current weak interactions or $\sim Z^2$ for EM dipole interactions, while incoherent processes dominate at higher energies or large $|t|$.⁶¹
- **Free protons**, as in hydrogen-rich materials, provide clean elastic up-scattering channels over a wide energy range. Inelastic contributions from bound nucleons, including nuclear excitations and breakup, become relevant in dense nuclear environments.^{63, 64}
- **Electrons** offer purely elastic, point-like scattering without form-factor suppression. Although the cross section is smaller due to the electron's low mass and absence of nuclear enhancement, this channel remains important in low threshold detectors with large electron densities.^{65, 66}

Overall, the neutrino up-scattering via the NDP is accessible over a wide range of energies and target materials. Its characteristic experimental signatures such as forward-peaked kinematics, displaced decays, and mono-photon final states make it a particularly promising channel for probing the NDP at both current and next-generation facilities.

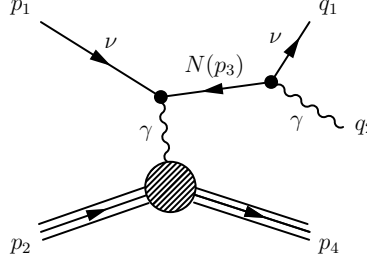


Fig. 1. Tree level neutrino scattering process with a final state photon, arising from dipole portal to HNL.³⁴

Dipole-induced differential cross sections for HNL production play a central role in describing neutrino up-scattering processes. They depend on both the recoil energy E_r of the final state target and the energy E_ν of the incoming neutrino. In general, the differential cross section is proportional to the contraction of a leptonic tensor $L_{\mu\nu}$ with a hadronic tensor $W^{\mu\nu}$. In terms of the right-handed projection operator, the leptonic tensor takes the form³⁴

$$L_{\mu\nu} = 4 \text{Tr} \left[\not{p}_1 P_R \sigma_{\nu\alpha} q^\alpha (\not{p}_3 + m_N) \sigma_{\mu\beta} q^\beta \right], \quad (6)$$

while the hadronic current is expressed as

$$\langle \mathcal{A} | \Gamma^\mu | \mathcal{A}' \rangle = F_1 \gamma^\mu + F_2 \frac{i}{2M_H} \sigma^{\mu\delta} q_\delta, \quad (7)$$

where F_1 and F_2 are form factors and M_H is the hadronic mass.

In the coherent regime, the neutrino scatters off the entire nucleus as a single object. The cross section then scales approximately as Z^2 (or A^2), and since $M_H = A M_{\text{nucleon}}$ with $|t| = |q^2| = Q^2$ small, only the F_1 term is retained in Eq. (7). In contrast, inelastic (incoherent) scattering occurs when the neutrino interacts with individual nucleons rather than the nucleus as a whole. In this case, $|t|$ is of moderate size, we set $M_H = M_{\text{nucleon}}$, and both F_1 and F_2 contribute. The form factors differ for protons and neutrons, with numerical values provided in Refs.^{34,67,68} Unlike the coherent case, the inelastic rate scales only linearly with Z or A , and the relevant kinematics avoid the forward scattering ($t \rightarrow 0$) enhancement characteristic of coherent scattering.

The explicit cross sections differ for electron and nuclear targets.³³ For electron scattering ($\nu e \rightarrow Ne$) one finds

$$\frac{d\sigma_\mu}{dE_r} = \alpha\mu_{\nu N}^2 \left[\frac{1}{E_r} - \frac{1}{E_\nu} + M_N^2 \frac{E_r - 2E_\nu - m_e}{4E_\nu^2 E_r m_e} + M_N^4 \frac{E_r - m_e}{8E_\nu^2 E_r^2 m_e^2} \right], \quad (8)$$

while for nuclear targets X_Z^A ($\nu X_Z^A \rightarrow N X_Z^A$),³³

$$\begin{aligned} \frac{d\sigma_\mu}{dE_r} = & \alpha\mu_{\nu N}^2 Z^2 F_1^2(E_r) \left[\frac{1}{E_r} - \frac{1}{E_\nu} + M_N^2 \frac{E_r - 2E_\nu - m_X}{4E_\nu^2 E_r m_X} + M_N^4 \frac{E_r - m_X}{8E_\nu^2 E_r^2 m_X^2} \right] \\ & + \alpha\mu_{\nu N}^2 \mu_X^2 F_2^2(E_r) \left[\frac{2m_X}{E_r^2} \left((2E_\nu - E_r)^2 - 2E_r m_X \right) + M_N^2 \frac{E_r - 4E_\nu}{E_\nu^2} + M_N^4 \frac{1}{E_\nu^2 E_r} \right], \end{aligned} \quad (9)$$

where M_N is the HNL mass, α the EM fine-structure constant, μ_X the nuclear magnetic moment, $\mu_{\nu N}$ the transition dipole moment, and m_X the target mass. At higher energies, nuclear substructure is partially resolved and coherence is lost, in which case both F_1 and F_2 are required. Magnetic moment contributions are typically negligible compared to the coherent Z^2 -enhanced term at low energies. For the nuclear charge form factor $F_1(E_r)$, we adopt the Helm parameterization,⁶⁹ which is practically equivalent to the symmetrized Fermi⁷⁰ and Klein–Nystrand⁷¹ forms.^a

The Helm form factor is given by⁶⁹

$$F_{\text{Helm}}(|\vec{q}|^2) = 3 \frac{j_1(|\vec{q}| R_0)}{|\vec{q}| R_0} e^{-|\vec{q}|^2 s^2 / 2}, \quad (10)$$

where $j_1(x) = (\sin x - x \cos x)/x^2$ is the spherical Bessel function of order one, $|\vec{q}| = \sqrt{2m_X E_r}$ is the magnitude of the three-momentum transfer for a recoil of energy E_r , and s is the nuclear skin thickness (typically $s = 1.0$ fm). The diffraction radius R_0 relates to the effective nuclear radius $R = 1.2 A^{1/3}$ fm by $R_0 = \sqrt{R^2 - 5s^2}$.

The kinematics further constrain the recoil spectrum. The minimum neutrino energy required to produce a recoil of energy E_r is

$$E_\nu^{\min}(E_r) = \frac{1}{2} \left[E_r + \sqrt{E_r^2 + 2m_X E_r} \right] \left(1 + \frac{M_N^2}{2E_r m_X} \right), \quad (11)$$

while the recoil spectrum vanishes below

$$E_r^{\min} = \frac{M_N^2}{2(m_X + M_N)}. \quad (12)$$

For fixed E_ν , the recoil spectrum peaks at

$$E_r^{\text{peak}}(E_\nu) = \frac{2m_X M_N^4}{8E_\nu^2 m_X^2 - 2m_X M_N^2 (2E_\nu + m_X) + M_N^4}, \quad (13)$$

^aWhile the Helm form is widely used for its simplicity, more accurate descriptions—such as Woods–Saxon⁷³ or Fourier–Bessel expansions—are recommended for heavy nuclei and experiments sensitive to detailed recoil spectra.⁷²

and the maximum recoil energy is

$$E_r^{\max}(E_\nu) = \frac{1}{2E_\nu + m_X} \left[E_\nu^2 - \frac{1}{2}M_N^2 + \frac{E_\nu}{2m_X} \left(\sqrt{M_N^4 - 4M_N^2m_X(E_\nu + m_X) + 4E_\nu^2m_X^2} - M_N^2 \right) \right]. \quad (14)$$

From these relations, one can see that producing a HNL via up-scattering off electrons requires a higher incoming neutrino energy than off nuclei of the same HNL mass. This is because the light electron absorbs a larger fraction of the recoil energy, reducing the phase space available for HNL production.⁷⁴

When the neutrino resolves individual nucleons rather than the entire nucleus, coherence is lost and the scattering becomes inelastic.^{61,62} In this regime, the momentum transfer $|t|$ is of moderate size, and the cross section scales linearly with the nucleon number ($\propto A$). The dynamics are governed by the nucleon form factors F_1 and F_2 , with the magnetic contribution in F_2 usually subdominant. Inelastic processes may excite discrete nuclear levels or lead to breakup into continuum states, though the rate is suppressed whenever the excitation energy $\Delta E \gtrsim E_r$. At sufficiently high neutrino energies, incoherent scattering on individual nucleons dominates. Explicit cross-section expressions are provided in Refs.,^{55,61} while more detailed treatments of nuclear response functions and structure effects can be found in Refs.^{48,75}

The neutrino up-scattering is a leading production mechanism for HNL across wide regions of parameter space and has been probed using data from LSND,⁷⁶ Mini-BooNE,⁷⁷ and the NOMAD single-photon search,⁷⁸ which have been recast to constrain dipole-mediated production and $N \rightarrow \nu\gamma$ decays. Future high intensity facilities, including SHiP⁷⁹ and the Short-Baseline Neutrino program (SBN),⁸⁰ are projected to achieve strong sensitivity.³⁴ Complementary bounds on the dipole coupling $\mu_{\nu N}$ arise from precision NEES, with results from GEMMA,^{81,84} TEXONO,^{82,83} Borexino,³⁷ and XENON1T.⁸⁵ Additional constraints come from CE ν NS, observed by COHERENT⁸⁶ and under active study at reactor-based experiments such as CONNIE⁸⁷ and CONUS.⁸⁸

3.2. Meson-Induced Production

In addition to neutrino up-scattering, HNLs can also be produced in meson decays via the NDP, providing unique and complementary channels beyond those associated with active-sterile mass mixing. These processes are particularly relevant in high intensity environments with abundant meson production, where both prompt and long-lived mesons may contribute depending on the experimental configuration. Dipole-induced meson decays can be classified into three main categories:⁸⁹

- Two-body decays of vector mesons,
- Radiative Dalitz-like decays of neutral pseudoscalar mesons,^{90–92}

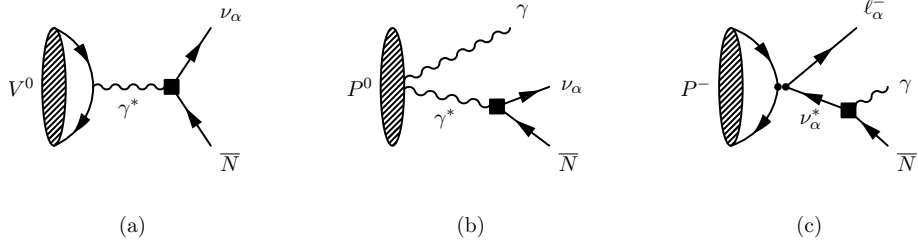


Fig. 2. Representative meson decay topologies induced by the NDP, taken from Ref.⁸⁹ : (a) Two-body vector meson decay, (b) Radiative Dalitz-like neutral meson decay, and (c) Weak three-body charged meson decay.

- Weak three-body decays of charged pseudoscalar mesons via off-shell neutrinos.

Each class corresponds to a distinct topology mediated by the dipole operator, as illustrated in Fig. 2, and exhibits characteristic kinematics and flavor dependence.

The relative importance of these modes depends on the experimental setup, in particular on how mesons are treated after production. In decay-pipe experiments (e.g. MiniBooNE,⁷⁷ SBN^{80,93}), long-lived charged mesons such as π^\pm and K^\pm dominate, since their decays in flight (DIFs) produce energetic HNLs that can reach downstream detectors. By contrast, short-lived neutral mesons (π^0 , η) decay promptly at the target. Although they can contribute through radiative dipole channels (e.g. $\pi^0 \rightarrow \gamma N \nu$), their limited boost and strongly forward-peaked final states typically make them subleading. In beam-dump experiments,^{94,95} absorption of long-lived charged mesons suppresses this contribution, shifting sensitivity toward prompt neutral meson decays. At colliders, heavy mesons such as D and B and light vector mesons (ρ^0 , ω , ϕ) are accessible, where rare dipole-induced decays in these channels can be reconstructed with high precision.^{96–98} The specific realizations of these three experimental configurations, decay-pipe, beam-dump, and collider setups, will be discussed in detail in the following sections. We now turn to specific meson decay modes that can produce HNLs via the dipole portal interaction.

3.2.1. Two-Body Decay of Vector Mesons

Flavorless vector mesons (V^0) like ρ^0 , ω , ϕ , J/ψ , and $\Upsilon(1S)$ can decay directly into a neutrino and an HNL via the dipole operator as shown in Fig. 2(a):

$$V^0 \rightarrow \nu_\alpha N. \quad (15)$$

This provides a clean and kinematically favorable channel to probe the NDP.⁸⁹ For a vector meson, one has

$$\langle 0 | \bar{q}_i \gamma^\mu q_j | V^0(p, \epsilon) \rangle = i f_V m_V \epsilon^\mu, \quad (16)$$

where m_V and f_V are the mass and the decay constant of V^0 , respectively, and ϵ^μ is its polarization vector. The decay width of interest reads⁸⁹

$$\Gamma(V^0 \rightarrow \nu_\alpha N) = \frac{f_V^2 m_V}{12\pi} e^2 Q_q^2 |\mu_{\nu N}|^2 \left(1 - \frac{M_N^2}{m_V^2}\right) \left(1 + \frac{M_N^2}{m_V^2} - 2 \frac{M_N^4}{m_V^4}\right), \quad (17)$$

where e is the electron charge, and Q_q is the charge (in units of e) of quark q composing V^0 . For light vector mesons such as ρ^0 , ω , and ϕ , the branching ratios are extremely small, $\text{BR} \lesssim 10^{-14}$ for $|\mu_{\nu N}| = 10^{-6} \text{ GeV}^{-1}$, owing to the combination of modest decay constants, EM coupling suppression, and large total widths.⁸⁹ As a result, the expected event yields in neutrino beam-dump or fixed-target experiments are negligible compared to dominant production channels such as neutrino up-scattering and radiative (Dalitz-like) pseudoscalar meson decays, which benefit from coherent Z^2 enhancement or large meson yields, respectively. This channel becomes potentially relevant only in environments with abundant heavy quarkonium production, such as forward LHC experiments (FASER/FASER2,⁹⁹ FACET¹⁰⁰), where narrow widths of states like J/ψ and Υ reduce the branching ratio suppression, or in scenarios where the HNL mass kinematically forbids lighter meson channels.

3.2.2. Radiative Dalitz-like Decays of Neutral Mesons

Neutral pseudoscalar mesons P^0 (e.g. π^0 , η) decay into two photons via the chiral anomaly. If one photon is off-shell, it can convert through the dipole operator into νN , leading to the three-body process $P^0 \rightarrow \gamma \nu N$ as shown in Fig. 2(b).^{34,89} This channel is directly induced by the NDP and is closely analogous to the standard Dalitz decay $P^0 \rightarrow \gamma \ell^+ \ell^-$.⁹⁰⁻⁹² A convenient representation of the amplitude is⁸⁹

$$i\mathcal{M} = \frac{e^2}{2\pi^2} \frac{\mu_{\nu N}}{f_P} \epsilon_\mu^* \epsilon^{\mu\nu\alpha\beta} \frac{g_{\nu\sigma}}{q^2} p_{2\alpha} q_\beta q_\rho [\bar{u}_\nu \sigma^{\rho\sigma} P_R v_N], \quad (18)$$

where f_P is the meson decay constant, p_2 is the momentum of the on-shell photon, and $q \equiv p_1 - p_2$ is the momentum of the virtual photon. Expressed in terms of the angle θ between the N and the real photon in the q -rest frame, the squared amplitude and the double differential width read⁸⁹

$$|\mathcal{M}|^2 = \frac{e^4}{32\pi^4} \frac{|\mu_{\nu N}|^2}{f_P^2} \frac{(q^2 - m_P^2)^2 (q^2 - M_N^2)}{q^4} \left[q^2 + 3M_N^2 - (q^2 - M_N^2) \cos 2\theta \right] \quad (19)$$

$$\frac{d^2\Gamma(P^0 \rightarrow \gamma \nu N)}{dq^2 d\cos\theta} = \frac{1}{512\pi^3 m_P} \left(1 - \frac{q^2}{m_P^2}\right) \left(1 - \frac{M_N^2}{q^2}\right) |\mathcal{M}|^2. \quad (20)$$

After integrating $q^2 \in [M_N^2, m_P^2]$ and $\cos\theta \in [-1, 1]$, one obtains the expected scaling $\Gamma(P^0 \rightarrow \gamma \nu N) \sim \alpha^2 \mu_{\nu N}^2 m_P^3 I(0, M_N^2/m_P^2)$, with a three-body phase space function $I(0, M_N^2/m_P^2)$ given by Eq.(A.5). Because the final-state photon is massless, the spectrum is forward-peaked and the mode remains sensitive up to the kinematic limit $M_N \simeq m_P$.

These Dalitz-like decays are most effectively probed in environments with abundant P^0 production and efficient photon reconstruction. Fixed-target kaon experiments (e.g. NA62) provide copious π^0 from $K^+ \rightarrow \pi^+ \pi^0$ decays,^{101,102} while collider detectors (Belle II, LHCb) can exploit high statistics samples of η , η' , and P^0 from heavy flavour and light hadron production, with excellent photon and vertexing performance.^{103–105}

3.2.3. Weak Three-Body Decays via Off-Shell Neutrino

Charged pseudoscalar mesons (P^\pm), such as π^\pm , K^\pm , D^\pm , D_s^\pm , and B^\pm , can decay into a charged lepton, photon, and HNL via an off-shell virtual neutrino, as shown in Fig. 2(c):^{34,89}

$$P^\pm \rightarrow \ell_\alpha^\pm (\nu_\alpha^* \rightarrow \gamma N). \quad (21)$$

This process proceeds through a charged-current weak interaction followed by a dipole mediated transition. It is flavor specific, enhanced for ν_μ due to the high flux of muon neutrinos in accelerator experiments, and is most relevant for low mass HNLs with $M_N \lesssim m_P - m_{\ell_\alpha}$. Such decays are loop-suppressed in the SM and are described via effective dipole operators. They have been discussed in the context of pion and kaon production in LSND, MiniBooNE, and SBN.³⁴

The process can be viewed as a rare three-body decay of the form

$$P^-(q) \rightarrow \ell^-(p_\ell) \gamma(k) N(p_N),$$

induced by an off-shell active neutrino transitioning into an HNL (N) via the dipole operator. The amplitude for $P^- \rightarrow \gamma \ell^- N$ is given schematically by⁸⁹

$$i\mathcal{M} = i 2\sqrt{2} G_F V_{ij} f_P \mu_{\nu N} \frac{1}{q^2} k_{1\alpha} \epsilon_\beta^* \left[\bar{u}_\ell \not{p}_1 \not{q} \sigma^{\alpha\beta} P_R v_N \right], \quad (22)$$

where G_F is the Fermi constant, V_{ij} is the relevant CKM element for $P^- \sim \bar{u}_i d_j$, and f_P is the decay constant defined through

$$\langle 0 | \bar{u}_i \gamma^\mu \gamma_5 d_j | P^-(p_1) \rangle = i f_P p_1^\mu.$$

Squaring the amplitude and expressing the scalar products in terms of the angle θ between the HNL and the charged lepton (ℓ_α) in the virtual neutrino rest frame, one finds⁸⁹

$$\begin{aligned} |\mathcal{M}|^2 = 8G_F^2 |V_{ij}|^2 f_P^2 |\mu_{\nu N}|^2 \frac{(q^2 - M_N^2)^2}{q^4} & \left[q^2(m_P^2 - q^2) + (2q^2 + m_P^2)m_{\ell_\alpha}^2 - m_{\ell_\alpha}^4 \right. \\ & \left. + (q^2 - m_{\ell_\alpha}^2) \sqrt{\lambda(q^2, m_P^2, m_{\ell_\alpha}^2)} \cos \theta \right], \end{aligned} \quad (23)$$

with λ the Källén function given by Eq.(A.4). The differential decay rate is then⁸⁹

$$\frac{d^2\Gamma(P^- \rightarrow \gamma \ell_\alpha^- N)}{dq^2 d\cos \theta} = \frac{\sqrt{\lambda(q^2, m_P^2, m_{\ell_\alpha}^2)}}{512\pi^3 m_P^3} \left(1 - \frac{M_N^2}{q^2}\right) |\mathcal{M}|^2, \quad (24)$$

with $q^2 \in [M_N^2, (m_P - m_{\ell_\alpha})^2]$ and $\cos \theta \in [-1, 1]$.

For charged pions, the integrated three-body decay width can be approximated as

$$\Gamma(\pi^- \rightarrow \mu^- \gamma N) \sim G_F^2 f_\pi^2 |V_{ud}|^2 |\mu_{\nu N}|^2 m_\pi^5 I(r_\mu, r_N), \quad (25)$$

where $r_\mu = m_\mu^2/m_\pi^2$, $r_N = M_N^2/m_\pi^2$. This scaling highlights that the dipole operator lifts the helicity suppression present in SM processes such as $\pi^- \rightarrow e^- \bar{\nu}$. The corresponding SM two-body rate is

$$\Gamma(\pi^- \rightarrow \mu^- \bar{\nu}) = \frac{G_F^2 |V_{ud}|^2 f_\pi^2 m_\pi m_\mu^2}{8\pi} \left(1 - \frac{m_\mu^2}{m_\pi^2}\right)^2,$$

and the approximate branching ratio can be written as

$$\text{BR}(\pi^- \rightarrow \mu^- \gamma N) \sim \frac{|\mu_{\nu N}|^2 m_\pi^4}{m_\mu^2} \frac{I(r_\mu, r_N)}{(1 - r_N)^2}. \quad (26)$$

Thus, the branching ratio scales quadratically with the dipole strength and is suppressed as $M_N \rightarrow m_\pi - m_\mu$.

Charged pseudoscalar mesons can also undergo rare *four-body* decays in which a virtual photon converts to a charged lepton pair via the dipole operator. The generic process is

$$M^+(q) \rightarrow \mu^+(p_\mu) \ell^+(p_+) \ell^-(p_-) N(p_N),$$

mediated by an off-shell neutrino ν^* that transitions into a HNL through the dipole interaction and radiates a virtual photon $\gamma^* \rightarrow \ell^+ \ell^-$.⁸⁹ This channel is universal across neutrino flavors and is relevant for HNL production in high-intensity facilities such as LSND, MiniBooNE, SBN, and SHiP. At leading order, the amplitude takes the schematic form

$$\mathcal{M} \sim \frac{G_F}{\sqrt{2}} V_{qq'} f_M \mu_{\nu N} \left[\bar{u}_\mu(p_\mu) \gamma^\alpha (1 - \gamma^5) \frac{p_\nu}{p_\nu^2} \sigma_{\rho\lambda} q'^\lambda P_R u_N(p_N) \right] \quad (27)$$

$$\times \frac{-g^{\rho\beta}}{q'^2} \left[\bar{u}_-(p_-) \gamma_\beta v_+(p_+) \right], \quad (28)$$

where $p_\nu = q - p_\mu$ is the off-shell neutrino momentum, $q' = p_+ + p_-$ the virtual photon momentum, and $\mu_{\nu N}$ is absorbed into the dipole vertex. The term $\bar{u}_- \gamma_\mu v_+$ represents the $\ell^+ \ell^-$ current. The complete four-body differential decay rate is given in Appendix A.3.

Introducing the invariant mass of the lepton pair, $m_{\ell\ell}^2 = q'^2 = (p_+ + p_-)^2$, the leading dependence of the spectrum can be written as

$$\frac{d\Gamma}{dm_{\ell\ell}^2} \propto \frac{G_F^2 f_M^2 |\mu_{\nu N}|^2 m_M^3}{m_{\ell\ell}^2} \lambda^{1/2} (m_M^2, m_\mu^2, M_N^2 + m_{\ell\ell}^2), \quad (29)$$

up to spinor-trace and angular factors. Here λ is the Källén function. The rate is enhanced at small $m_{\ell\ell}$ due to the $1/q'^2$ photon propagator, while the phase space closes at the endpoint $m_M < m_\mu + M_N + 2m_\ell$. The $m_{\ell\ell}$ spectrum is therefore sharply peaked near threshold, $m_{\ell\ell} \simeq 2m_\ell$, mimicking an ordinary Dalitz decay.^{90–92} The

differential full four-body decay rate is defined in Appendix A.3. A rough parametric estimate of the branching ratio (neglecting angular integrals) can be obtained by treating the four-body mode as the three-body radiative decay multiplied by the probability for $\gamma^* \rightarrow \ell^+ \ell^-$ conversion. Following the analysis of Dalitz decays,^{90–92} one finds

$$\text{BR}(M \rightarrow \mu \ell^+ \ell^- N) \sim \frac{\alpha}{3\pi} \text{BR}(M \rightarrow \mu \gamma N) \log\left(\frac{m_M^2}{m_\ell^2}\right), \quad (30)$$

where the logarithm reflects the collinear enhancement in $\gamma^* \rightarrow \ell^+ \ell^-$, regulated by the lepton mass m_ℓ . In contrast to the three-body radiative mode, which yields a broad photon energy spectrum, the four-body channel exhibits a sharp peak in the dilepton invariant-mass distribution near $m_{\ell\ell} \simeq 2m_\ell$.

3.3. Production at Colliders

Collider experiments provide a complementary probe of the NDP, offering clean kinematics and extending sensitivity to higher HNL masses than fixed-target facilities. At the partonic level, the leading dipole-mediated process is

$$e^+ e^- \rightarrow \gamma^* \rightarrow \nu N \text{ (or } \bar{\nu} N\text{)}, \quad (31)$$

with a differential cross section⁵⁴

$$\frac{d\sigma}{d \cos \theta_N} = \frac{\mu_{\nu N}^2 \alpha (s - M_N^2)^2 [(1 - \cos^2 \theta_N) s + (1 + \cos^2 \theta_N) M_N^2]}{4s^3}, \quad (32)$$

where θ_N is the HNL scattering angle. The total cross section is

$$\sigma(e^+ e^- \rightarrow \nu N) = \frac{\mu_{\nu N}^2 \alpha (s - M_N^2)^2 (s + 2M_N^2)}{3s^3}. \quad (33)$$

The two-body final state νN is experimentally invisible, being indistinguishable from the SM background $e^+ e^- \rightarrow \nu \bar{\nu}$. Searches therefore focus on the radiative channel

$$e^+ e^- \rightarrow \nu N \gamma, \quad (34)$$

where the photon is emitted either from the initial state or directly at the dipole vertex. The additional photon provides a clean trigger and efficiently suppresses the otherwise overwhelming $e^+ e^- \rightarrow \nu \bar{\nu}$ background. Facilities such as Belle II⁹⁷ and BESIII⁹⁶ are sensitive to HNLs with $m_N \sim 10\text{--}500$ MeV, probing both mono-photon plus missing energy ($\gamma + \cancel{E}_T$) signatures and displaced photons from long-lived N decays.

At LEP, mono-photon searches for $e^+ e^- \rightarrow \gamma + \cancel{E}_T$ were carried out by ALEPH and OPAL, setting limits on anomalous neutral-current processes and thereby constraining dipole couplings up to M_N near the electroweak scale.^{106,107} At the LHC ($\sqrt{s} = 13\text{--}14$ TeV), the analogous process arises via Drell–Yan production,

$$q \bar{q} \rightarrow \gamma^* \rightarrow \nu N, \quad (35)$$

followed by $N \rightarrow \nu\gamma$, which yields the characteristic $\gamma + \not{E}_T$ topology. ATLAS and CMS have performed mono-photon searches exploiting isolated high- p_T photons accompanied by large missing energy to suppress SM backgrounds.^{108,109} Subleading photon-initiated processes such as $\gamma q \rightarrow Nq$ may also contribute but are suppressed, while $\gamma\gamma \rightarrow \nu N$ requires two dipole insertions and is negligible compared to the Drell-Yan channel.

In summary, collider production probes the NDP through electroweak processes tagged by photons: Belle II⁹⁷ and BESIII⁹⁶ cover the sub-GeV mass window, LEP^{106,107} constrained up to tens of GeV, and the LHC^{108,109} extends sensitivity into the multi-GeV regime.

4. Experimental Signatures

Experimental probes of the NDP rely on two qualitatively different classes of observable signatures. First, if the HNL is produced on shell, it will eventually decay radiatively via $N \rightarrow \nu\gamma$, yielding a photon signal that may appear promptly, with a displaced vertex, or with a measurable time delay. These decay-based signatures are the hallmark of beam-dump, fixed-target, and collider experiments searching for long-lived particles. Second, even in the absence of visible decays, dipole interactions can manifest as distortions in recoil energy spectra from elastic scattering processes such as NEES or CE ν NS. In this case, the signal consists of an excess of low energy recoils relative to the expectation, driven by the characteristic $1/E_r$ enhancement of the dipole contribution.^{48,55} We then expect that these complementary strategies, through both decay signatures and recoil distortions, cover a wide range of lifetimes, energies, and detector technologies, providing a unified framework to test the NDP.

4.1. Radiative Decay Signatures

The produced HNL decays radiatively via $N \rightarrow \nu\gamma$, with width⁴⁶

$$\Gamma(N \rightarrow \nu\gamma) = \frac{|\mu_{\nu N}|^2 M_N^3}{4\pi}. \quad (36)$$

This dominant two-body decay produces an active neutrino and a photon. The corresponding lab-frame decay length is³⁴

$$L_{\text{dec}} = \frac{E_N}{M_N} \cdot \frac{1}{\Gamma(N \rightarrow \nu\gamma)} = \frac{4\pi E_N}{|\mu_{\nu N}|^2 M_N^4}, \quad (37)$$

where E_N is the HNL energy. For example, taking $E_N = 100$ GeV, $M_N = 150$ MeV, and $\mu_{\nu N} = 10^{-6}$ GeV⁻¹ gives $L_{\text{dec}} \sim 490$ m.

In high-density detector, the signal photon typically converts into a detectable e^+e^- pair, while in low-density detectors the rare three-body decay $N \rightarrow \nu e^+e^-$ (via a virtual photon, branching ratio $\sim 0.6\%$ ¹¹⁰) may be easier to identify owing to reduced neutrino-induced backgrounds. Depending on the dipole coupling and the HNL mass, the decay can be prompt or occur with a displaced vertex inside the detector. The $N \rightarrow \nu\gamma$ mode can therefore manifest experimentally as:

- **Prompt decays:** Photons appear at the primary vertex with no resolvable displacement ($L \ll$ detector resolution). These are kinematically indistinguishable from SM backgrounds such as $\pi^0 \rightarrow \gamma\gamma$, bremsstrahlung, or radiative meson decays. Experimental handles include parent-meson tagging (e.g. $K^+ \rightarrow \ell^+ N$), mono-photon plus missing energy searches, deviations in photon spectra, or fast timing. Experiments with clean environments and kinematic control (NA62,¹⁰¹ LSND,⁷⁶ MiniBooNE,⁷⁷ Belle II⁹⁷) are especially sensitive.
- **Displaced decays:** For lifetimes in the cm–100 m range, photons originate away from the primary vertex, producing a striking, low-background signal. Identification relies on photon conversion or angular pointing. This signature is ideal for beam-dump and fixed-target experiments (SHiP,⁷⁹ FASER,¹¹¹ MiniBooNE beam dump mode,³⁵ FACET¹⁰⁰), and can also be probed at colliders for sub-meter displacements.
- **Delayed decays:** Even if the displacement is unresolved, delayed photon arrival can occur when the HNL travels before decaying. Observing this requires sub-ns timing. ATLAS,¹¹² CMS,¹¹³ DUNE,¹¹⁴ and proposed setups such as FACET¹⁰⁰ could be sensitive. This regime extends coverage to very long lifetimes but demands excellent timing and background rejection.

The probability that an HNL decays within a fiducial region bounded by L_1 and L_2 from the production point is¹¹⁵

$$P_{\text{dec}}(L_1, L_2) = \exp\left(-\frac{L_1}{L_{\text{dec}}}\right) - \exp\left(-\frac{L_2}{L_{\text{dec}}}\right), \quad (38)$$

with L_{dec} the lab-frame decay length. This formula applies both in long-baseline neutrino setups (T2K,¹¹⁶ DUNE,¹¹⁷ MiniBooNE³⁵) and in collider or beam-dump experiments (Belle II,¹⁰³ LHC, FASER,¹¹¹ SHiP¹¹⁸). For prompt decays, $L_{\text{dec}} \ll$ detector dimensions, giving $P_{\text{dec}} \simeq 1$. The dominant radiative channel $N \rightarrow \nu\gamma$ produces a single energetic photon, forward-collimated by the HNL boost and accompanied by little additional activity. Sensitivity therefore depends on photon acceptance and reconstruction efficiency. Adequate angular and energy resolution are needed to separate signal photons from neutral-current backgrounds.

For neutrino up-scattering production, the expected number of events is

$$N_{\text{event}} = N_T \int dE_r \frac{dR}{dE_r} \text{BR}(N \rightarrow \nu\gamma) P_{\text{dec}} \epsilon_{\text{geo}} \epsilon_{\text{rec}}, \quad (39)$$

where N_T is the number of targets, dR/dE_r is the differential rate,¹¹⁹ and ϵ_{geo} , ϵ_{rec} are the geometric and reconstruction efficiencies. For meson production, the analogous expression is¹¹⁵

$$N_{\text{event}} = \sum_{\mathcal{M}} N_{\mathcal{M}} \text{BR}(\mathcal{M} \rightarrow NX) \text{BR}(N \rightarrow \nu\gamma) P_{\text{dec}} \epsilon_{\text{sel}}, \quad (40)$$

where ϵ_{sel} is the photon-selection efficiency and $N_{\mathcal{M}}$ the number of mesons produced,

$$N_{\mathcal{M}} = \begin{cases} N_{\text{POT}} f_{\mathcal{M}}, & \text{for fixed-target experiments (NA62,\sup{101,120} HIKE,\sup{121} SHiP\sup{118})}, \\ \sigma_{pp} \mathcal{L} f_{\mathcal{M}}, & \text{for colliders (FASER2\sup{99})}. \end{cases} \quad (41)$$

Here N_{POT} is the number of protons on target, σ_{pp} the inelastic proton–proton cross section, \mathcal{L} the integrated luminosity, and $f_{\mathcal{M}}$ the average meson multiplicity.

4.2. Recoil Spectrum Distortions

In neutrino scattering experiments probing the NDP, the signal is not a visible decay of HNL, but instead a distortion of the recoil energy spectrum compared to the SM prediction. In particular, NEES and CE ν NS offer clean channels where dipole interactions add an extra contribution to the cross section. The characteristic feature of this contribution is an enhancement at low recoil energies, scaling approximately as $1/E_r$, which stands in sharp contrast to the SM predictions. Below we outline the formalism for the recoil spectra in both NEES and CE ν NS channels, emphasizing how neutrino up-scattering via the dipole operator modifies the event rates measured in detectors.

4.2.1. NEES

The SM prediction for flavor α and neutrino energy E_{ν} is⁵⁵

$$\frac{d\sigma_{\nu_{\alpha}e}^{\text{SM}}}{dE_r} = \frac{2G_F^2 m_e}{\pi} \left[g_L^2 + g_R^2 \left(1 - \frac{E_r}{E_{\nu}} \right)^2 - g_L g_R \frac{m_e E_r}{E_{\nu}^2} \right], \quad (42)$$

where E_r is the electron recoil kinetic energy, m_e is the electron mass, and

$$g_L(\nu_e) = \frac{1}{2} + \sin^2 \theta_W, \quad g_L(\nu_{\mu,\tau}) = -\frac{1}{2} + \sin^2 \theta_W, \quad g_R = \sin^2 \theta_W, \quad (43)$$

For antineutrinos, $g_L \leftrightarrow g_R$. The expected number of recoil events in an energy bin i is then

$$N_i = N_e \int_{E_r^i}^{E_r^{i+1}} dE_r \epsilon(E_r) \int_{E_{\min}(E_r)}^{E_{\max}} dE_{\nu} \frac{d\Phi_{\nu}}{dE_{\nu}} \frac{d\sigma_{\nu e}^{\text{tot}}}{dE_r}(E_{\nu}, E_r), \quad (44)$$

where $N_e = Z N_{\text{target}}$ is the number of electrons, $\epsilon(E_r)$ the detection efficiency, and $d\Phi_{\nu}/dE_{\nu}$ the incident neutrino flux. The minimum neutrino energy required to produce a recoil of E_r is given in Eq. (12).

Different neutrino experiments implement the detector efficiency $\epsilon(E_r)$ in distinct ways. In the GEMMA experiment,⁸¹ based on a high-purity germanium detector at the Kalinin Nuclear Power Plant, the detection efficiency near threshold is determined using pulse calibrations. The effective energy threshold has been reported as low as $E_{\text{th}} \simeq 2.8$ keV, and the efficiency curve around this threshold is measured

rather than modeled with a closed analytic form.^{81,84} For Borexino, the large liquid-scintillator volume provides nearly unity efficiency above $E_r \gtrsim 150$ keV, thanks to its exceptionally high light yield and precise calibration procedures that reconstruct electron recoils directly in keV_{ee}.¹²² In TEXONO experiment,³⁸ which employs a CsI(Tl) scintillating crystal array exposed to reactor antineutrinos, the overall efficiency in the 3–8 MeV recoil window is approximately constant at $\epsilon \simeq 0.77$. This value is obtained after applying event-selection criteria such as cosmic-ray veto, multi-hit rejection, and fiducial-volume cuts, with only mild residual energy dependence across this range.^{38,82}

Then, the total differential cross section in the presence of the NDP is simply given by

$$\frac{d\sigma_{\nu e}^{\text{tot}}}{dE_r} = \frac{d\sigma_{\nu e}^{\text{SM}}}{dE_r} + \frac{d\sigma_{\nu e}^{\text{NDP}}}{dE_r}. \quad (45)$$

where the dipole contribution exhibits a $1/E_r$ enhancement at low recoil energy.

4.2.2. CE ν NS

The SM prediction for the differential cross section of CE ν NS with a spin-zero nucleus \mathcal{N} with Z protons and N neutrons as a function of the nuclear kinetic recoil energy E_r is given by^{123–125}

$$\frac{d\sigma_{\nu_\alpha - \mathcal{N}}}{dE_r}(E_\nu, E_r) = \frac{G_F^2 m_{\mathcal{N}}}{\pi} \left(1 - \frac{m_{\mathcal{N}} E_r}{2E_\nu^2}\right) Q_{\alpha, \text{SM}}^2, \quad (46)$$

where G_F is the Fermi constant, the index α denotes the neutrino flavor, E_ν is the neutrino energy, $m_{\mathcal{N}}$ is the mass of nucleus and $Q_{\alpha, \text{SM}} = [g_V^p(\nu_\alpha) Z F_Z(|\vec{q}|^2) + g_V^n(\nu_\alpha) N F_N(|\vec{q}|^2)]$. For neutrino-proton coupling, g_V^p and the neutrino-neutron coupling, g_V^n , we can take;²⁶ $g_V^p(\nu_e) = 0.0401$, $g_V^n(\nu_\mu) = 0.0318$, and $g_V^n = 0.0401$. In Eq. (46), $F_Z(|\vec{q}|^2)$ and $F_N(|\vec{q}|^2)$ are, respectively, the form factors of the proton and neutron distributions in the nucleus, respectively. The Helm form factor is given by Eq.(10). The nucleon charge radius is given by $R_{p(n)}^2 = \frac{3}{5} R_0^2 + 3s^2$ with R_p and R_n are the rms radii of the proton and neutron distributions, respectively, The size of the neutron distribution radius R_n is taken to be 4.7 fm and 4.1 fm for the analyses involving CsI and Ar, respectively.¹²⁶ Note that the coherence is lost for $|\vec{q}|R_{p(n)} \gtrsim 1$

The theoretical prediction of CE ν NS event-number N_i in each nuclear-recoil energy-bin i is given by¹²⁷

$$N_i = N(\mathcal{N})_D \int_{E_r^i}^{E_r^{i+1}} dE_r f(n_{\text{PE}}(E_r)) \int_{E_{\text{min}}}^{E_{\text{max}}} dE \sum_{\nu=\nu_e, \nu_\mu, \bar{\nu}_\mu} \frac{d\Phi_\nu}{dE} \frac{d\sigma_{\nu_\alpha - \mathcal{N}}}{dE_r}(E, E_r) \quad (47)$$

where $f(n_{\text{PE}})$ is the energy-dependent reconstruction efficiency, $E_{\text{max}} = m_\mu/2 \sim 52.8$ MeV, N_D represents the number of target nuclei in the detector mass and is

given by $N_D = g_{\text{mol}} \frac{m_{\text{det}} N_A}{(m_{\mathcal{N}})_{\text{mol}}}$ where m_{det} is the detector mass, N_A is the Avogadro's number, $(m_{\mathcal{N}})_{\text{mol}}$ is the molar mass of the detector molecule and g_{mol} is the number of atoms in a single detector molecule. For CsI detector,^{128,129} $m_{\text{det}} = 14.6$ kg and $(m_{\text{CsI}})_{\text{mol}} = 259.8$ gram/mol, and for Ar detector,⁸⁶ $m_{\text{det}} = 24$ kg and $(m_{\text{Ar}})_{\text{mol}} = 39.96$ gram/mol. The lower integration limit in Eq. (47) E_{min} is the minimum neutrino energy required to attain a recoil energy E_r , which is given by Eq.(12).

The reconstruction efficiency for CsI detector is given in terms of the detected number of photoelectrons n_{PE} by the function¹²⁹

$$f(n_{\text{PE}}) = \frac{a}{1 + \exp(-k(n_{\text{PE}} - n_0))} \Theta(n_{\text{PE}} - 5), \quad (48)$$

where $a = 0.6655^{+0.0212}_{-0.0384}$, $k = 0.4942^{+0.0335}_{-0.0131}$, $n_0 = 10.8507^{+0.1838}_{-0.3995}$, and the function $\Theta(x)$ is defined as $0(x < 5)$, $0.5(5 \leq x < 6)$, $1(x \geq 6)$. For Ar detector, we take the detector efficiency from the results in Ref.⁸⁶ For CsI detector, we consider the quenching factor,¹²⁹

$$n_{\text{PE}} = 1.17 \left(\frac{E_r}{\text{keV}_{\text{nr}}} \right), \quad (49)$$

describing the number of photo-electrons detected by photo-multiplier tubes per keV nuclear recoil energy. It can be used to map n_{PE} to the recoil energy E_r in the analysis. For Ar detector, the electron-equivalent recoil energy $T_{\text{ee}}[\text{keV}_{\text{ee}}]$, is transformed into the nuclear recoil energy $E_r[\text{keV}_{\text{nr}}]$ thanks to the relation⁸⁶

$$T_{\text{ee}} = f_Q(E_r)E_r, \quad (50)$$

where f_Q is the quenching factor, which is the ratio between the scintillation light emitted in the nuclear and electron recoils. It is parameterised as $f_Q(E_r) = (0.246 \pm 0.006 \text{ keV}_{\text{nr}}) + ((7.8 \pm 0.9) \times 10^{-4})E_r$ up to 125 keV_{nr}, and is kept constant for larger values.⁸⁶ Note that the two functions $f(n_{\text{PE}})$ and $f_Q(E_r)$ play different roles in the analysis. The quenching factor $f_Q(E_r)$ encodes the scintillation response of the detector medium, mapping the true nuclear recoil energy E_r to the electron-equivalent visible energy T_{ee} . In contrast, the reconstruction efficiency $f(n_{\text{PE}})$ describes the probability that an event with a given number of photoelectrons n_{PE} is successfully triggered and recorded by the detector.

The differential cross section for the up-scattering process, $\nu_L + \mathcal{N} \rightarrow N + \mathcal{N}$, is given by^{33,34,130,131}

$$\frac{d\sigma}{dE_r} = \alpha \mu_{\nu N}^2 Z^2 F_N^2 (|\vec{q}|^2) \left[\frac{1}{E_r} - \frac{1}{E_\nu} + M_N^2 \frac{E_r - 2E_\nu - m_{\mathcal{N}}}{4E_\nu^2 E_r m_{\mathcal{N}}} + M_N^4 \frac{E_r - m_{\mathcal{N}}}{8E_\nu^2 E_r^2 m_{\mathcal{N}}^2} \right], \quad (51)$$

where $\mu_{\nu N}$ are common for all flavors. From Eq.(14), we can obtain the maximum possible recoil energy for a given neutrino energy E_ν by replacing M_T with $m_{\mathcal{N}}$. In the analysis, M_N is taken so that E_r^{max} becomes larger than E_r^i for a given range of E_ν in eq.(47). We find that the most conservative upper limit on M_N satisfying

$E_r^{\max} \gtrsim E_r^i$ is about 40 MeV, which is taken as an upper limit for the scan of M_N in our analysis. The presence of Z^2 scaling (as opposed to N^2) and the infrared divergence at low E_r distinguish this contribution from the SM background.

5. Experimental Searches and Constraints

Based on the experimental signatures discussed in Sec. 4, we now turn to the corresponding searches and constraints.

(i) *Fixed-target accelerator experiments*, in which intense neutrino beams from meson decays enable production or up-scattering of heavy states. This class includes the short-baseline anomalies (LSND,¹³² MiniBooNE⁷⁷) as well as dedicated scattering measurements (CHARM-II,¹³³ NOMAD,¹³⁴ DONUT,¹³⁵ T2K¹³⁶).

(ii) *High-energy neutrino probes*, which extend sensitivity to the highest accessible energies. These include collider searches, where e^+e^- or hadronic collisions produce heavy states accompanied by photons (LEP mono-photon studies^{106, 107}), and astrophysical observatories such as IceCube,¹³⁷ which detect atmospheric and astrophysical neutrinos up to the PeV scale.

(iii) *Recoil-based detectors*, where low energy neutrino scattering produces measurable recoils. This category covers NEES with solar and reactor fluxes (Borexino,³⁷ Super-Kamiokande,¹³⁸ GEMMA,⁸⁴ TEXONO,³⁸ XENON1T⁸⁵) and CE ν NS, first observed with accelerator neutrinos by COHERENT¹²⁸ and now also probed at reactors (CONUS+,¹³⁹ Dresden-II¹⁴⁰) and in multi-ton dark-matter detectors pursuing solar neutrino CE ν NS (XENONnT,³⁹ PandaX-4T,⁴⁰ LZ⁴¹).

These complementary approaches span wide ranges in energy, baseline, and lifetime, thereby mapping out the experimentally accessible parameter space of the NDP. Table 1 summarizes the main experimental probes of the NDP, listing the neutrino source, dominant flavor sensitivity, key observables, and the accessible mass-lifetime range. It highlights the complementarity of different approaches: solar and reactor experiments constrain the sub-MeV regime through recoil spectra, accelerator facilities probe the MeV–GeV range via up-scattering and photon signatures, and colliders and neutrino observatories extend reach to the multi-GeV and astrophysical scales. In what follows, we present the current exclusion results and the projected sensitivities achievable at future experiments, as illustrated in Figs. 3–5. Unless noted otherwise, *shaded regions* or *solid curves* denote existing 90–95% C.L. exclusions, while *dashed curves* indicate future sensitivities. When multiple analyses overlap, only the combined envelope is shown. Figure 3 (electron flavor) presents results in the $(M_N, \mu_{\nu_e N})$ plane, with analogous constraints for ν_μ and ν_τ given in Figs. 4 and 5. In these figures, the left panels display current exclusions, while the right panels show the same plots with projected sensitivities overlaid as dashed curves.

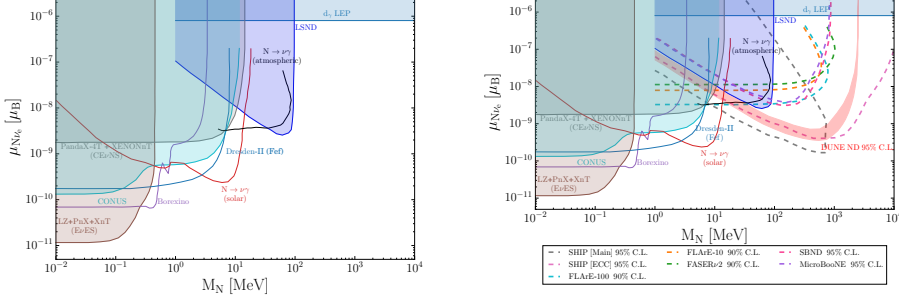


Fig. 3. Constraints on the (M_N, μ_{NeN}) parameter space for ν_e . **Left:** Current 90–95% C.L. exclusions from reactor NEES (CONUS,⁸⁸ Dresden-II,¹⁴⁰ GEMMA,^{81,84} TEXONO³⁸), solar NEES searches (Borexino,³⁷ SK¹³⁸), LSND,¹³² and dark matter detectors (XENONnT,³⁹ PandaX-4T,⁴⁰ LZ⁴¹). **Right:** Same as left panel, with the addition of the new CONUS+ bound (including CEvNS and NEES),^{139,141} and projected sensitivities from DUNE-ND,¹¹⁷ SHiP,⁷⁹ FASER ν 2,⁹⁹ and FLArE-10/100.¹⁰⁰

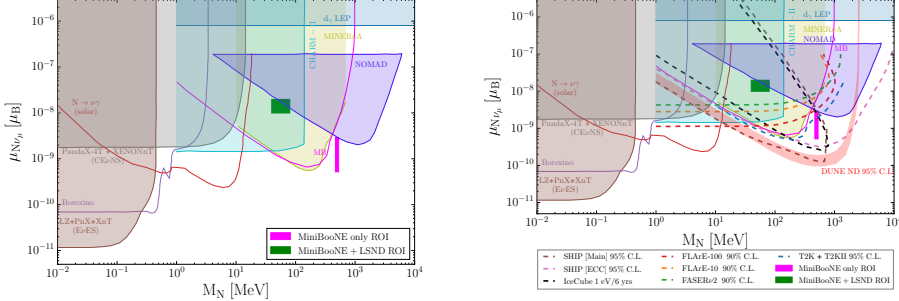


Fig. 4. Constraints on the $(M_N, \mu_{\mu N})$ parameter space for ν_μ . **Left:** Current 90–95% C.L. exclusions from CHARM-II,¹³³ NOMAD,¹³⁴ MINER ν A,¹⁴⁹ Borexino, and MiniBooNE/LSND, along with CEvNS and NEES limits from Fig. 3. **Right:** Same as the left panel, with the addition of projected sensitivities from T2K+T2K-II,¹¹⁶ DUNE-ND,¹¹⁷ SHiP,¹¹⁸ FASER ν 2,⁹⁹ FLArE-10/100,¹⁰⁰ and IceCube.¹³⁷ ROIs motivated by the MiniBooNE anomaly⁷⁷ are also shown.

5.1. LSND and MiniBooNE anomalies

Both LSND and MiniBooNE were short-baseline *fixed-target* experiments originally designed for oscillation studies. Their anomalous e -like signals have been reinterpreted as possible dipole-induced upscattering followed by radiative decays, motivating early bounds on the NDP. However, careful recasts of their data now show that the dipole explanation of these anomalies is strongly disfavored.

[LSND experiment]: The dark blue region labeled "LSND" in Fig. 3 shows the 95% C.L. exclusion obtained from LSND's precise NEES measurement³⁴ in the dipole-portal parameter space. Within the NDP framework, ν_e from μ^+ DAR (and

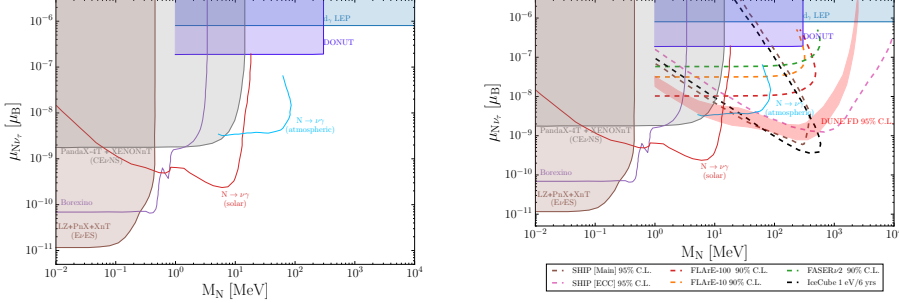


Fig. 5. Constraints on the $(M_N, \mu_{\nu_\tau N})$ parameter space for ν_τ . **Left:** Existing 90–95% C.L. exclusions from DONUT,¹³⁵ solar NEES searches, reactor and CE ν NS searches with xenon detectors, and radiative decay bounds from solar/atmospheric neutrinos. **Right:** Same as the left panel, with the addition of the projected reach of DUNE-FD,¹¹⁴ SHIP,¹¹⁸ FASER ν 2,⁹⁹ FLArE-10/100,¹⁰⁰ and IceCube,¹³⁷ which provide sensitivity to long-lived radiative decays in the ν_τ sector.

subleading ν_μ from π DIF) can upscatter on electrons via the dipole interaction, and the produced N decays radiatively, yielding single-photon e -like Cherenkov signatures.^{142,143} Because LSND had sensitivity to both ν_e and ν_μ components of the DAR/DIF flux, the analysis provides complementary exclusions in both the electron– and muon–flavor dipole couplings. But, the LSND bound is shown in the electron–flavor panels, since its strongest sensitivity arises from ν_e produced in μ^+ decay at rest.

[MiniBooNE experiment]: The **MiniBooNE** experiment observed an excess of low energy e -like events,⁷⁷ motivating dipole interpretations^{142–144} in which ν_μ upscatters to N and the subsequent $N \rightarrow \nu\gamma$ decay mimics an e -like signal. Unlike LSND, the MiniBooNE flux was overwhelmingly dominated by ν_μ from pion DIF, so its analysis constrains only the muon–flavor dipole coupling. The solid magenta curve labeled "MB" in Fig. 4 shows a 95% C.L. exclusion from binned fits to the published E_ν^{QE} and $\cos\theta$ distributions,¹⁴⁵ restricted to $E_\nu^{\text{QE}} > 475$ MeV and using a shape–only fit for $\cos\theta$ with profiled normalization.³⁴ These bounds strongly disfavour the dipole explanation across a wide mass–coupling range. The "MiniBooNE–only" and "MiniBooNE+LSND" ROIs highlighted in Fig. 4 are now tightly constrained by LSND NEES and MiniBooNE anomaly–free data.³⁴

5.2. Accelerator–based neutrino experiments

Beyond the anomalies, additional *fixed-target* accelerator experiments set strong constraints on dipole couplings, as summarized below.

[Existing Exclusions]: In Fig. 4, **CHARM-II**¹³³ and **NOMAD**¹³⁴ provide the leading 95% C.L. bounds on the ν_μ – N dipole coupling.^{119,146} The cyan shaded region corresponds to the CHARM-II exclusion, derived from precision measurements of $\nu_\mu e^- \rightarrow \nu_\mu e^-$ scattering, where dipole effects enhance the low-recoil spec-

trum. The dark blue shaded region denotes the NOMAD exclusion, obtained from its dedicated single-photon search that probes dipole-induced neutrino up-scattering followed by $N \rightarrow \nu\gamma$. We note that these two results are complementary: CHARM-II constrains the low-recoil regime, while NOMAD probes the sub-GeV mass range via photon signatures.^{119,146–148} In addition, the **MINERvA** experiment has recently provided complementary constraints. Using the NuMI beam at Fermilab, MINERvA performed a search for dipole-induced single-photon signatures arising from neutrino up-scattering followed by $N \rightarrow \nu\gamma$.¹⁴⁹ No excess above background was observed, leading to a 95% C.L. exclusion, shown as the yellow shaded regions in Fig. 4, which further restricts the dipole portal parameter space in the sub-GeV mass range. This result is complementary to those from CHARM-II and NOMAD, providing coverage that lies between their respective sensitivity regions. In the left panel of Fig. 5, **DONUT**¹³⁵ sets the first direct accelerator limit on $\mu_{\nu_\tau N}$ through $\nu_\tau e^-$ scattering, shown as the dark blue shaded region.^{119,146}

A constraint has also been derived from the **T2K ND280** (2019) dataset.¹¹⁶ Dipole-induced upscattering $\nu A \rightarrow N A$ with subsequent $N \rightarrow \nu\gamma \rightarrow e^+ e^-$ decays was searched for in the electron-like sample. The resulting exclusion disfavors part of the parameter space proposed as a dipole-portal explanation of the MiniBooNE anomaly, already ruling out the combined energy- and angular-distribution region at 95% C.L.¹⁵⁰ However, the ND280 contour is not included in Fig. 3, since its reach is concentrated in this anomaly motivated window, while broader coverage at low and intermediate masses is already provided by LSND and by reactor/solar experiments.¹⁵⁰

[Projected Sensitivities]: In the right panel of Fig. 4, the *projected T2K+T2K-II* sensitivity¹⁵⁰ is shown as a blue dashed contour. Because the J-PARC beam is ν_μ -dominated, the future projections are displayed in the muon-flavor panel. The proposed **SHiP** experiment at the CERN SPS¹¹⁸ will probe $\mu_{\nu N}$ using both the main decay volume (Main) and the emulsion cloud chamber (ECC). The projected sensitivities appear in all three right panels as dashed curves: light brown for the Main volume and pink for the ECC.³⁴ Production from prompt mesons and dipole-induced upscattering enables lifetime-wedge coverage up to $\mathcal{O}(\text{GeV})$. At Fermilab, **DUNE** will provide complementary reach.¹¹⁷ In the right panels of Figs. 3 and 4, the *near detector* sensitivity is shown as a filled red contour at 95% C.L., probing the neutrino up-scattering with prompt photon-like signatures from $N \rightarrow \nu\gamma$. In the right panel of Fig. 5, the *far detector* extends coverage to displaced $N \rightarrow \nu\gamma$ decays, probing longer lifetimes and larger M_N .¹¹⁴ Forward LHC detectors, **FASER** ν/ν^2 ⁹⁹ and proposed **FLArE-10/100**,¹⁰⁰ further extend the reach using TeV-scale neutrino fluxes from pp collisions. Their 90% C.L. sensitivities are shown by the green dashed curves for FASER $\nu/2$ in each panel, and by the orange (red) dashed curves for FLArE-10(100), covering higher energies and complementing the SPS and LBNF facilities. We note that the anomaly-motivated *MiniBooNE-only ROI* and the combined *MiniBooNE+LSND ROI* highlighted in the right panel of Fig. 4 can be tested by the blue dashed T2K+T2K-II projection and the red

DUNE-ND region, with the ND280 exclusion already disfavoring the joint energy- and angular-distribution region at 95% C.L..¹⁵⁰

5.3. Low-energy NEES experiments

Recoil-based detectors provide leading constraints through low energy NEES, as discussed below.

[Solar neutrino experiments]: Low threshold electron recoil measurements by **Borexino**¹⁵¹ and **Super-Kamiokande (SK)**¹³⁸ provide strong bounds on the ν_e dipole portal through distortions in the recoil spectrum from solar $\nu_e e \rightarrow Ne$ scattering with subsequent $N \rightarrow \nu\gamma$. In Borexino,¹⁵¹ a dedicated fit to the low energy spectrum yields the strongest sensitivity for $m_N \lesssim 10$ MeV, where neutrino up-scattering is kinematically open; above this range, sensitivity falls rapidly, and the limits are dominated by the ν_e coupling. In Fig. 3, the purple curve labeled “Borexino” represents this exclusion. SK extends coverage to higher solar neutrino energies, and the **combined Borexino+SK analysis**³² further strengthens exclusions across the MeV regime by incorporating both low- and high-energy recoil data. This bound is shown by the red curve labeled “ $N \rightarrow \nu\gamma$ (solar)” in Fig. 3, constraining $\mu_{\nu_e N}$ over the $m_N \sim$ MeV range.

The **XENON1T** experiment⁸⁵ has derived complementary constraints on the dipole portal from the measured low energy electron recoil spectrum. Dipole-induced scattering would lead to an excess of events in the sub-keV to few-keV range, which is not observed. The resulting 90% C.L. exclusion removes additional parameter space in the ν_μ dipole sector, as indicated by the blue-shaded region labeled “Xenon1T” in Fig. 6.¹¹⁹ The **SuperCDMS**¹⁵² experiment is projected to achieve 90% C.L. sensitivity to the dipole interaction with sub-keV thresholds and ton-year exposures. As indicated by the black dashed curve labeled “SuperCDMS” in Fig. 6,¹¹⁹ its reach extends well into the sub-MeV mass regime, fully covering the exclusion obtained from XENON1T and further lowering the bound to $\mu_{\nu N} \sim 10^{-8}$ GeV⁻¹. In contrast to Borexino and SK, which constrain only the electron-flavor coupling through solar ν_e scattering, the XENON1T limit and the projected SuperCDMS sensitivity are presented identically in all flavor panels under the assumption that only one dipole coupling is nonzero at a time.

[Reactor neutrino experiments]: Reactor-based $\bar{\nu}_e e^-$ scattering experiments provide complementary probes of the ν_e dipole coupling. The **TEXONO** experiment,^{82,83} using low-threshold germanium detectors, measures $\bar{\nu}_e e^-$ scattering where an NDP contribution would appear as the characteristic $1/E_e$ enhancement in the recoil spectrum. The resulting exclusion, shown as the green-shaded region in Fig. 6, constrains the dipole portal coupling in the sub-MeV to MeV mass range at 90% C.L..^{153,154} The **GEMMA** experiment,⁸⁴ employing a high-purity germanium detector with very low recoil thresholds, is particularly sensitive to dipole-induced $\bar{\nu}_e e \rightarrow Ne$ scattering. Here, the dipole interaction would enhance the event rate at sub-keV recoil energies. The absence of such an excess yields world leading limits

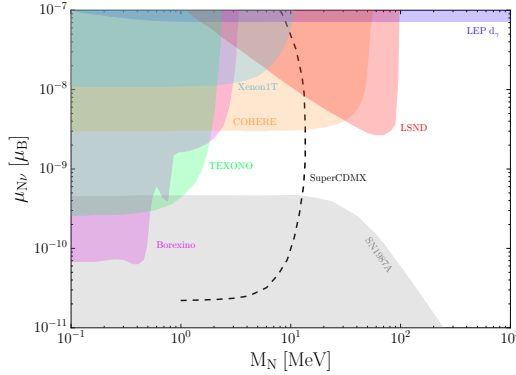


Fig. 6. Constraints on the (M_N, μ_{ν_N}) parameter space, assuming only one dipole coupling is nonzero at a time. Current 90–95% C.L. exclusions are shown from XENON1T¹¹⁹(blue), COHERENT¹²⁸(yellow), and TEXONO³⁸(green), with additional comparisons to Borexino¹⁵¹(pink) and LSND¹³²(red). The projected sensitivity of SuperCDMS¹⁵² (black dashed) and the exclusion from SN1987A³⁴ (grey) are also shown.

in the light mass regime, corresponding to $\mu_{\nu_e N} \lesssim \text{few} \times 10^{-11} \mu_B$ at 90% C.L..¹⁵⁴

5.4. CE ν NS Experiments

CE ν NS provides a flavor blind probe of the NDP in principle, owing to the universal nuclear response, but current measurements constrain only $\mu_{\nu_e N}$ and $\mu_{\nu_\mu N}$, since available fluxes come from reactors ($\bar{\nu}_e$) and stopped-pion sources ($\nu_\mu, \bar{\nu}_\mu, \nu_e$).

[COHERENT at the SNS]: The **COHERENT** program at the Spallation Neutron Source (SNS) has provided the first and most detailed CE ν NS measurements using multiple detector technologies.¹⁵⁵ The SNS neutrino flux consists of monoenergetic ν_μ at 29.9 MeV from π^+ decay at rest (DAR) and continuous ν_e and $\bar{\nu}_\mu$ spectra extending up to 52.8 MeV from μ^+ decay. In the NDP, CE ν NS cross sections receive dipole-induced enhancements that modify the recoil spectrum in a flavor dependent way: ν_μ constraints are driven by the monoenergetic line, while ν_e and $\bar{\nu}_\mu$ limits follow from the DAR continuum. The first CE ν NS observation with a CsI[Na] detector established the signal³⁶ and provided the initial exclusion on μ_{ν_N} under the assumption that only one dipole coupling is nonzero, as shown by the yellow-shaded region in Fig. 3.^{127,153} Follow-up measurements with liquid argon (CENNS-10)⁸⁶ and NaI¹⁵⁶ confirmed the effect and provided complementary constraints using different nuclear targets and systematics. Future germanium based detectors are expected to extend sensitivity to sub-keV recoils.¹⁵⁵

[Reactor CE ν NS]: Reactor-based experiments probe ν_e dipole couplings at much lower energies. The **Dresden-II** germanium detector has searched for $\bar{\nu}_e + \text{Ge} \rightarrow N + \text{Ge}$, applying an ON/OFF likelihood analysis that incorporates reactor flux, exposure, quenching modeled via the iron–filter method, and detector

response.¹⁴⁰ The resulting 90% C.L. exclusion rules out a significant portion of the $(M_N, \mu_{\nu_e N})$ parameter space, shown by the blue curve labeled “Dresden-II (Fef)” in Fig. 3. The recent **CONUS+** results,^{139, 141} obtained with sub-keV thresholds, further strengthen these bounds. Under a single-flavor ν_e dipole hypothesis, the cyan solid curve in Fig. 3 denotes the 90% C.L. exclusion boundary, with the shaded region above it illustrating the corresponding excluded parameter space. A characteristic feature of both Dresden-II and CONUS+ is the flat behavior at $M_N \ll E_\nu$, followed by a rise near $M_N \sim \text{few} \times 10$ MeV, reflecting the interplay of CE ν NS kinematics, the reactor $\bar{\nu}_e$ spectrum, and nuclear form factors. Together, Dresden-II and CONUS+ provide the strongest reactor based CE ν NS exclusions on $\mu_{\nu_e N}$.

[Dual-phase xenon TPCs]: Large dark matter detectors such as **XENONnT**,³⁹ **PandaX-4T**,⁴⁰ and **LZ**⁴¹ also measure CE ν NS from solar neutrinos, in addition to NEES. From Figs. 3–5, the combined XENONnT+PandaX-4T CE ν NS analysis yields an upper bound of $\mu_{\nu N} \lesssim 1.5 \times 10^{-10} \mu_B$, while the joint LZ+XENONnT+PandaX-4T NEES analysis improves this limit to $\mu_{\nu N} \lesssim 1.5 \times 10^{-11} \mu_B$.¹⁵⁷ In the panels, these constraints are represented by the grey-shaded region (XENONnT+PandaX-4T CE ν NS) and the light-brown-shaded region (LZ+XENONnT+PandaX-4T NEES), both indicating the corresponding excluded parameter space. In the exclusion panels, CE ν NS curves exhibit an almost vertical cutoff at $M_N \sim 10\text{--}15$ MeV, while NEES bounds cut off around 3–4 MeV, both set by the kinematic endpoint of the ^8B solar-neutrino spectrum. At sub-MeV masses, CE ν NS limits from these multi-ton TPCs surpass Borexino’s reach, offering unprecedented sensitivity to light dipole portals.

5.5. High-energy neutrino probes (LEP and IceCube)

At the highest energies, both a collider (LEP) and an astrophysical neutrino observatory (IceCube) probe the NDP through high energy neutrino production and up-scattering.

[Collider searches (LEP)]: At the Z pole, the **LEP** experiments searched for single-photon plus missing-energy events, $e^+e^- \rightarrow \gamma + \cancel{E}$,¹⁰⁶ with similar analyses later extended to higher energies at **LEP2**.¹⁰⁷ Within the NDP framework, this channel receives contributions from $e^+e^- \rightarrow \nu N \gamma$, where the photon can arise either from initial-state radiation or directly from the dipole vertex. Recasts of the LEP datasets in this context place stringent bounds on the dipole portal coupling $\mu_{\nu N}$.³⁴ In the panels, the blue regions enclosed by solid blue lines (shown for $\mu_{\nu N} = 9 \times 10^{-7} \mu_B$) indicate the 95% C.L. exclusion for a pure EM dipole operator.

[IceCube]: High-energy atmospheric and astrophysical neutrinos traversing the **IceCube** detector¹³⁷ can undergo dipole-induced upscattering, $\nu e \rightarrow Ne$, with the heavy state subsequently decaying radiatively, $N \rightarrow \nu \gamma$. Such processes would manifest as EM cascades, and may produce distinctive double-bang-like topologies if the upscattering and decay vertices are spatially separated.¹⁴⁶ A recast of IceCube data¹³⁷ reports no excess above the expected background, leading to 95% C.L. ex-

clusions. These are shown as the black dashed lines in the right panels of Fig. 4 and Fig. 5,¹⁴⁶ corresponding to the same constraint represented by the blue dashed curve in Fig. 6. These bounds are most constraining at large M_N and high energies, where the TeV-to-PeV neutrino flux provides maximal sensitivity. As illustrated in Ref.,¹⁴⁶ the black dashed curves correspond to double-bang constraints derived from the atmospheric neutrino flux, normalized to the expectation of one visible event over six years of data taking.

LEP and IceCube provide complementary high-energy probes of the NDP: LEP delivers leading exclusions in the sub-100 GeV mass range through e^+e^- collisions at the Z pole, while IceCube extends sensitivity to much larger M_N by exploiting atmospheric and astrophysical neutrino fluxes.

5.6. Cosmological Constraints (BBN and CMB)

Cosmology constrains the NDP primarily through Big Bang Nucleosynthesis (BBN) and the Cosmic Microwave Background (CMB). Dipole-mediated interactions such as $\nu\gamma \rightarrow N$ and $f^+f^- \rightarrow N\nu$ (with f a SM fermion) can thermalize heavy neutral leptons in the early Universe at rates $\propto |\mu_{\nu N}|^2$.³⁴ Once produced, their abundance and decay history determine their cosmological impact. During BBN ($T \sim 0.1$ –1 MeV), additional relativistic degrees of freedom increase the Hubble rate and modify light-element yields, while late decays ($\tau_N \gtrsim 1$ s) inject entropy and distort the baryon-to-photon ratio and deuterium abundance.¹⁵⁸ Consistency with observations of primordial ${}^4\text{He}$ and deuterium therefore requires that N either decouples early, decays early ($\tau_N \ll 1$ s), or never thermalizes. Analyses of light-element abundances, including precise D/H measurements from quasar absorption spectra¹⁵⁹ and the helium fraction Y_p inferred from CMB data ($Y_p = 0.243^{+0.023}_{-0.024}$ at 95% C.L. from Planck TT,TE,EE+lowE+lensing+BAO⁴⁴), constrain the effective number of relativistic species to $\Delta N_{\text{eff}}^{\text{BBN}} \lesssim 0.3$ – 0.4 .^{44, 160, 161} For light HNL, this implies $\mu_{\nu N} \lesssim \mathcal{O}(10^{-10}) \mu_B$, ensuring decoupling before BBN.¹⁶²

At recombination ($T \sim 0.26$ eV), the CMB provides a complementary bound on extra relativistic relics. The effective contribution is given by^{160, 163–165}

$$\Delta N_{\text{eff}} = \frac{g_N}{2} \left(\frac{T_N}{T_\nu} \right)^4 = \frac{g_N}{2} \left(\frac{10.75}{g_{*,s}(T_{\text{decouple}})} \right)^{4/3} \quad (52)$$

where we have used $g_{*,s}(T_\nu) \simeq 10.75$ at the neutrino decoupling temperature T_ν . The *Planck* 2018 results combined with BAO yield $N_{\text{eff}}^{\text{obs}} = 2.99 \pm 0.17$ at 68% C.L.,⁴⁴ consistent with the SM prediction $N_{\text{eff}}^{\text{SM}} = 3.045$,¹⁶² corresponding to $\Delta N_{\text{eff}} \lesssim 0.3$ at 95% C.L. Taken together, BBN and CMB require $\mu_{\nu N} \lesssim \mathcal{O}(10^{-10}) \mu_B$ for m_N up to a few–tens of MeV, ensuring early decoupling or rapid decay. The exclusion labeled “Cosmology” in Fig. 7 summarizes the envelope of constraints derived from BBN and CMB observations¹⁵⁷

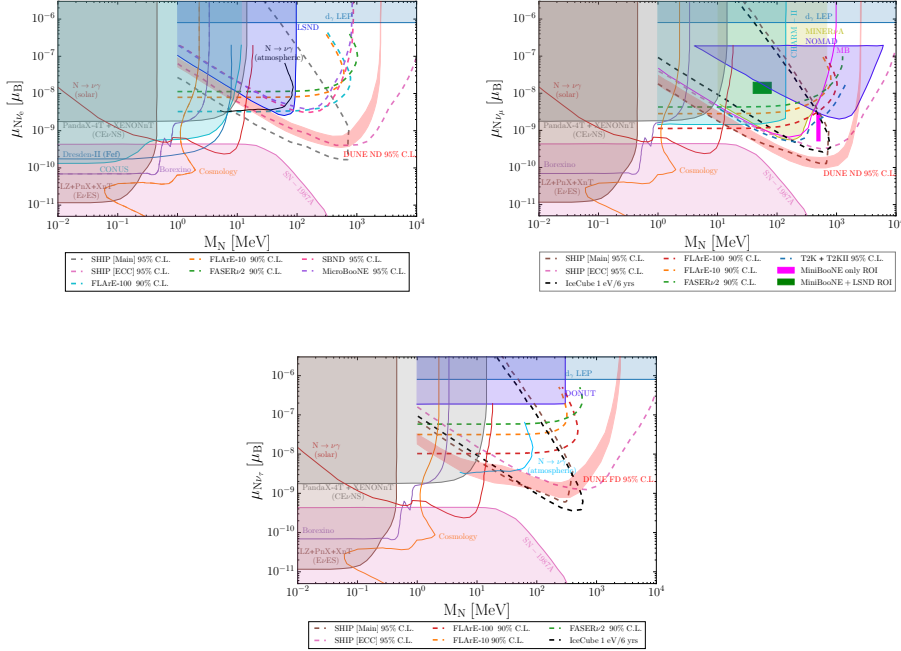


Fig. 7. Cosmological and astrophysical exclusions on the dipole portal parameter space, overlaid on the right panels of Figs. 3–5. Each panel shows the 95% C.L. exclusion labeled “Cosmology,” summarizing BBN and CMB bounds on ΔN_{eff} that exclude $\mu_{\nu N} \gtrsim 10^{-10} \mu_B$ for $m_N \lesssim \mathcal{O}(10)$ MeV.¹⁵⁷ Also shown is the “SN1987A” region, derived from the ~ 10 s neutrino burst observed by Kamiokande-II,¹⁶⁹ IMB,¹⁷⁰ and Baksan,¹⁷¹ which constrains excessive energy loss from dipole-induced HNL emission.¹⁵⁷

5.7. Astrophysical Constraints from SN1987A

Core-collapse supernovae probe the dipole portal through energy–loss arguments. In SN1987A, the proto–neutron star reached $T \sim 30$ MeV and nuclear densities $\rho \sim 3 \times 10^{14}$ g/cm³, enabling prolific N production through NEES and plasmon decay.^{34, 57, 58} If HNL couples too weakly, it free-streams out of the star, accelerating cooling beyond the observed ~ 10 s neutrino burst.^{58, 166} If instead it couples too strongly, its mean free path shrinks and HNL becomes trapped, thermalizing with the plasma and decoupling from a new neutrinosphere.^{167, 168} The observed burst duration in **Kamiokande-II**,¹⁶⁹ **IMB**,¹⁷⁰ and **Baksan**¹⁷¹ matched expectations from SM neutrino diffusion, leaving little room for additional exotic losses.

Imposing the Raffelt criterion⁵⁷ on the exotic emissivity yields an approximate upper bound for light HNLs ($m_N \lesssim 100$ MeV):

$$\mu_{\nu N} \lesssim (1-3) \times 10^{-9} \mu_B.$$

At larger couplings, the free–streaming bound no longer applies; this defines a trap-

ping window around

$$10^{-8} \mu_B \lesssim \mu_{\nu N} \lesssim 10^{-6} \mu_B,$$

where constraints weaken.³⁴ The shaded “SN1987A” regions in Fig. 7 summarize this interplay of free-streaming and trapping, excluding a broad band of parameter space for $m_N \lesssim 100$ MeV that is otherwise unconstrained by laboratory data.¹⁵⁷

6. Conclusion and Outlook

The NDP represents a minimal but powerful extension of the SM neutrino sector. Through a single higher-dimensional operator, it links active neutrinos to HNLs and the EM field, generating a wide spectrum of novel phenomena: radiative decays, single-photon and displaced-photon signatures, and characteristic distortions in electron and nuclear recoil spectra. Because the same operator governs production, decay, and scattering, the NDP provides a unifying framework in which laboratory, astrophysical, and cosmological probes all converge.

Over the past decade, an impressive range of experiments has constrained this framework. Short-baseline anomalies at LSND and MiniBooNE motivated early dipole-portal interpretations, now largely excluded by accelerator scattering data from CHARM-II, NOMAD, MINERvA, and T2K ND280. Recoil-based measurements such as Borexino, SK, Dresden-II, and CONUS+ probe the low-mass regime, while multi-ton xenon and argon TPCs have pushed sensitivities to unprecedented levels. At the highest energies, LEP and IceCube provide complementary exclusions, while astrophysical and cosmological arguments from SN1987A, BBN, and the CMB close off large regions of parameter space. Together, these inputs have already constrained $\mu_{\nu N}$ down to $\sim 10^{-11} \mu_B$ for HNL masses below $\mathcal{O}(10)$ MeV.

Several forthcoming developments are expected to define the next decade of exploration. Next-generation long-baseline experiments such as DUNE and Hyper-Kamiokande will combine near and far detector capabilities to probe both recoil distortions and displaced radiative decays. High energy frontier experiments including SHiP, FASER ν 2, and FLArE will extend coverage into the multi-GeV regime, complementing astrophysical probes. At lower energies, Dresden-II, CONUS+, and upcoming sub-keV threshold detectors (e.g., SuperCDMS) will further test the sub-MeV mass range. Dark matter detectors such as XENONnT, PandaX-4T, and LZ, though designed for other purposes, will continue to play a leading role in probing light sterile states via CE ν NS and NEES. On the cosmological and astrophysical side, improved BBN and CMB analyses, together with the next galactic supernova, promise to refine bounds on the dipole portal far beyond current laboratory reach.

The overall picture is one of complementarity. Accelerator programs are closing gaps in the sub-GeV to multi-GeV window; reactor and solar experiments dominate the sub-MeV regime; and astrophysical and cosmological probes guarantee coverage across and beyond laboratory sensitivities. This multi-pronged approach ensures that the most phenomenologically viable regions of parameter space will be either robustly excluded or tested with discovery potential in the near future.

In conclusion, the NDP provides a rare example of a simple, predictive, and highly testable framework that bridges energy, intensity, astrophysical, and cosmological frontiers. Its exploration constrains HNL scenarios, illuminates possible connections to hidden sectors, and sharpens our understanding of neutrino EM properties. The next generation of experiments and observations will determine whether the NDP remains a powerful constraint on new physics models, or emerges as the first confirmed window into dynamics beyond the SM.

Acknowledgments

This work was supported by the Research Program funded by the Seoul National University of Science and Technology.

Appendix A. Formulae for Decay Rate

Appendix A.1. Two-body Decay

For two-body decay, the decay rate is calculated by

$$\Gamma_{fi} = \frac{p^*}{32\pi^2 m_a^2} \int |\mathcal{M}_{fi}|^2 d\Omega, \quad (\text{A.1})$$

where $p^* = \frac{1}{2m_a} \sqrt{[m_a^2 - (m_1 + m_2)^2][m_a^2 - (m_1 - m_2)^2]}$.

The HNL decays into a neutrino and a gamma via the NDP interaction, whose decay rate is given by

$$\Gamma_{N \rightarrow \nu\gamma} = \frac{|\mu_{\nu N}|^2 M_N^3}{4\pi}, \quad (\text{A.2})$$

Using the decay rate, we can calculate the decay length and lifetime of N . For an HNL energy of $E_N = 1 \text{ GeV} \gg M_N$, the decay length (L_{dec}) and lifetime of N (τ_N) in lab-framework scale as

$$\begin{aligned} L_{\text{dec}} &= c\tau\beta\gamma \approx 2500m \left(\frac{10 \text{ MeV}}{M_N} \right)^4 \left(\frac{10^{-6} \text{ GeV}^{-1}}{d} \right)^2, \\ \tau_N &= \tau\gamma = 8.13 \times 10^{-4} \text{s} \left(\frac{10 \text{ MeV}}{M_N} \right)^4 \left(\frac{10^{-6} \text{ GeV}^{-1}}{d} \right)^2, \end{aligned} \quad (\text{A.3})$$

where τ is the proper lifetime of N , and γ, β its Lorentz boost factors. This turns out to be a very convenient length scale for beam dump experiments, if M_N and $\mu_{\nu N}$ have the fiducial values suggested above.

Appendix A.2. Three-body Decay

We start from the total decay width for a three-body process:

$$X(p) \rightarrow a(p_1) + b(p_2) + c(p_3),$$

given by:

$$\Gamma = \frac{1}{(2\pi)^3} \frac{1}{32m_X^3} \int |\mathcal{M}|^2 dm_{ab}^2 dm_{bc}^2. \quad (5)$$

Our goal is to express the differential decay rate with respect to m_{ab}^2 by integrating over m_{bc}^2 :

$$\frac{d\Gamma}{dm_{ab}^2} = \frac{1}{(2\pi)^3} \frac{1}{32m_X^3} \int |\mathcal{M}(m_{ab}^2, m_{bc}^2)|^2 dm_{bc}^2. \quad (6)$$

This form holds when the squared amplitude depends on two Mandelstam-like variables, $m_{ab}^2 = (p_1 + p_2)^2$ and $m_{bc}^2 = (p_2 + p_3)^2$.

Appendix A.2.1. Integration Limits for m_{bc}^2

For fixed m_{ab}^2 , the kinematically allowed range for m_{bc}^2 is given by:

$$(m_{bc}^2)_{\min} \leq m_{bc}^2 \leq (m_{bc}^2)_{\max},$$

with the limits determined by solving the energy-momentum constraints and triangle inequalities. These can be expressed using the Källén function:¹⁷⁸

$$\lambda(a, b, c) = a^2 + b^2 + c^2 - 2ab - 2ac - 2bc. \quad (\text{A.4})$$

Appendix A.2.2. Loop/Phase-Scape Function

The dimensionless loop/phase-space function for three-body decay ($\pi^+ \rightarrow \mu^+ \gamma N$) is typically given by:¹⁷⁹

$$I(r_\mu, r_N) = \int_{r_\mu^2}^{(1-r_N)^2} dx \frac{(x - r_\mu^2)}{x^3} \sqrt{\lambda(1, x, r_N^2)} F(x), \quad (\text{A.5})$$

where $x = E_\gamma/m_\pi$ is the rescaled photon energy, $r_\mu = m_\mu/m_\pi$, $r_N = m_N/m_\pi$, $\lambda(a, b, c)$ is the Källén function given by Eq.(A.4), arising from phase space, $F(x)$ is a loop integrand factor (from the virtual neutrino propagator and dipole form), which typically behaves like x or $1/x$ depending on the operator structure.

Appendix A.3. Four-body Decay

The differential full four-body decay rate is given by:

$$d\Gamma = \frac{1}{2m_M} |\mathcal{M}|^2 d\Phi_4, \quad (\text{A.6})$$

where the four-body phase space is:

$$d\Phi_4 = (2\pi)^4 \delta^{(4)}(q - p_\mu - p_N - p_+ - p_-) \prod_{i=1}^4 \frac{d^3 p_i}{(2\pi)^3 2E_i}. \quad (\text{A.7})$$

Appendix A.3.1. *Example: $\pi^+ \rightarrow \ell^+ \gamma \nu$*

Define a dimensionless photon energy variable:

$$x = \frac{2E_\gamma}{m_\pi}, \quad 0 \leq x \leq 1 - r_\ell^2, \quad r_\ell = \frac{m_\ell}{m_\pi}.$$

The squared matrix element $|\mathcal{M}|^2$ typically depends on x and can be integrated as:

$$\frac{d\Gamma}{dx} = \frac{1}{(2\pi)^3} \frac{1}{32m_\pi} \int |\mathcal{M}(x)|^2 d\cos\theta,$$

where θ is the angle between ℓ^+ and γ in the pion rest frame. The differential rate may involve functions like $\lambda^{1/2}(1, x, r_\nu^2)$ and dipole factors such as $F(x) \sim 1/x$ or x .

Experiment	Neutrino source	Flavor sensitivity	Observable / strategy	M_N reach & lifetime
Borexino	Solar ($p p$, 7 Be, 8 B)	Mainly ν_e (CC-enhanced)	e recoil spectrum, distortion	$\lesssim 10$ MeV; prompt
Borexino+SK	Solar (^8B + higher- E)	ν_e dominated	Low+high- E recoil spectra	$\lesssim 15$ MeV; prompt
Super-K (atm. ν)	Atmospheric (GeV)	ν_e , ν_μ , ν_τ via osc.	Up-scattering + $N \rightarrow \nu\gamma$	0.1–10 GeV; displaced or prompt
IceCube	Atm / astro (TeV–PeV)	All flavors (oscillated)	γ/e -like events from $N \rightarrow \nu\gamma$	\gtrsim GeV–TeV; long-lived
Xe1T/ PnX / LZ	Solar ($p p$, 8 B)	Flavor blind (CE ν NS)	Electron recoil + CE ν NS	$\lesssim 10$ –15 MeV; prompt
SuperCDMS	Solar (low- E)	Mainly ν_e , flavor blind	Sub-keV electron recoils	Sub-MeV–few MeV; prompt
Dresden-II	Reactor $\bar{\nu}_e$	ν_e only	CE ν NS upscattering on Ge	$\lesssim 10$ MeV; prompt
COHERENT	SNS (29.9 MeV $\nu_{(\mu, e)}$, $\bar{\nu}_\mu$)	ν_μ , ν_e , $\bar{\nu}_\mu$	CE ν NS + recoil spectrum	$\lesssim 50$ MeV; prompt
LSND	Accelerator (30 MeV νe)	ν_e	ν_e ES	$\lesssim 50$ MeV; prompt
MINIBOONE	Booster ν_μ beam (GeV)	ν_μ , ν_e contamination	e -like events from $N \rightarrow \nu\gamma$	~ 0.1 –GeV prompt+upstream
CHARM-II	SPS ν_μ	ν_μ	ν_μ – e ES	\sim GeV scale; prompt
NOMAD	SPS ν_μ	ν_μ	ν_μ – e ES, mono- γ search	GeV scale; prompt
DUNE ND	LBNF beam (GeV)	ν_μ dominated, all flavors	$\nu e \rightarrow N e$ then $N \rightarrow \nu\gamma$	0.1–GeV; prompt
DUNE FD	LBNF beam (GeV)	Mixed flux after osc.	Displaced $N \rightarrow \nu\gamma$; long-lived	
SHiP ECC	SPS (400 GeV p beam)	ν_μ dominated	High-res. $N \rightarrow \nu\gamma$	0.1–GeV; short-lived
SHiP Main	SPS beam dump	ν_μ dominated	mono- γ from $N \rightarrow \nu\gamma$	0.1–GeV; long-lived
LEP (91 GeV)	$e^+ e^-$ at Z-pole	Flavor independent	mono- γ + E_T	~ 10 –100 GeV; prompt

Table 1. Classification of experimental bounds on the NDD.

References

- Y. Fukuda *et al.* [Super-Kamiokande], Phys. Rev. Lett. **81**, 1562-1567 (1998) doi:10.1103/PhysRevLett.81.1562 [arXiv:hep-ex/9807003 [hep-ex]].
- Q. R. Ahmad *et al.* [SNO], Phys. Rev. Lett. **89**, 011301 (2002) doi:10.1103/PhysRevLett.89.011301 [arXiv:nucl-ex/0204008 [nucl-ex]].
- K. Eguchi *et al.* [KamLAND], Phys. Rev. Lett. **90**, 021802 (2003) doi:10.1103/PhysRevLett.90.021802 [arXiv:hep-ex/0212021 [hep-ex]].
- P. Minkowski, “ $\mu \rightarrow e\gamma$ at a Rate of One Out of 10^9 Muon Decays?,” Phys. Lett. B **67**, 421 (1977). doi:10.1016/0370-2693(77)90435-X
- M. Gell-Mann, P. Ramond and R. Slan sky, *Supergravity*, ed. by D. Freedman and P. Van Nieuwenhuizen, North Holland, Amsterdam, 315 (1979)
- T. Yanagida, *Proc. of the Workshop on the Unified Theory and Baryon Number in the Universe*, ed. by O. Sawada and A. Sugamoto (KEK report 79-18), 95 (1979)
- R. N. Mohapatra and G. Senjanovic, “Neutrino Mass and Spontaneous Parity Nonconservation,” Phys. Rev. Lett. **44**, 912 (1980). doi:10.1103/PhysRevLett.44.912
- J. Schechter and J. W. F. Valle, “Neutrino Masses in $SU(2) \times U(1)$ Theories,” Phys. Rev. D **22**, 2227 (1980). doi:10.1103/PhysRevD.22.2227
- A. Zee, “A Theory of Lepton Number Violation, Neutrino Majorana Mass, and Oscillation,” Phys. Lett. B **93**, 389 (1980) [erratum: Phys. Lett. B **95**, 461 (1980)]. doi:10.1016/0370-2693(80)90349-4
- E. Ma, “Verifiable radiative seesaw mechanism of neutrino mass and dark matter,” Phys. Rev. D **73**, 077301 (2006). doi:10.1103/PhysRevD.73.077301 [arXiv:hep-ph/0601225]
- N. Arkani-Hamed, S. Dimopoulos, G. R. Dvali and J. March-Russell, Phys. Rev. D **65**, 024032 (2001) doi:10.1103/PhysRevD.65.024032 [arXiv:hep-ph/9811448 [hep-ph]].
- E. Ma, M. Raidal and U. Sarkar, Phys. Rev. Lett. **85**, 3769-3772 (2000) doi:10.1103/PhysRevLett.85.3769 [arXiv:hep-ph/0006046 [hep-ph]].
- C. Giunti and T. Lasserre, Ann. Rev. Nucl. Part. Sci. **69**, 163-190 (2019) doi:10.1146/annurev-nucl-101918-023755 [arXiv:1901.08330 [hep-ph]].
- S. K. Kang, Int. J. Mod. Phys. A **34**, no.10, 1930005 (2019) doi:10.1142/S0217751X19300059 [arXiv:1904.07108 [hep-ph]].
- B. Dasgupta and J. Kopp, Phys. Rept. **928**, 1-63 (2021) doi:10.1016/j.physrep.2021.06.002 [arXiv:2106.05913 [hep-ph]].
- M. Escudero, N. Rius and V. Sanz, JHEP **02**, 045 (2017) doi:10.1007/JHEP02(2017)045 [arXiv:1606.01258 [hep-ph]].
- M. Escudero, N. Rius and V. Sanz, Eur. Phys. J. C **77**, no.6, 397 (2017) doi:10.1140/epjc/s10052-017-4963-x [arXiv:1607.02373 [hep-ph]].
- P. Ballett, M. Hostert and S. Pascoli, Phys. Rev. D **101**, no.11, 115025 (2020) doi:10.1103/PhysRevD.101.115025 [arXiv:1903.07589 [hep-ph]].
- S. Böser, C. Buck, C. Giunti, J. Lesgourgues, L. Ludhova, S. Mertens, A. Schukraft and M. Wurm, Prog. Part. Nucl. Phys. **111**, 103736 (2020) doi:10.1016/j.ppnp.2019.103736 [arXiv:1906.01739 [hep-ex]].
- J. E. Kim, [arXiv:1911.06883 [hep-ph]].
- J. Jeong, J. E. Kim and S. Youn, [arXiv:2105.01842 [hep-ph]].
- J. E. Kim, Phys. Rev. D **14**, 3000 (1976) doi:10.1103/PhysRevD.14.3000
- For a review, see C. Giunti and A. Studenikin, Rev. Mod. Phys. **87**, 531 (2015) doi:10.1103/RevModPhys.87.531 [arXiv:1403.6344 [hep-ph]].
- K. Fujikawa and R. Shrock, “The Magnetic Moment of a Massive Neutrino and Neutrino Spin Rotation,” Phys. Rev. Lett. **45**, 963 (1980). doi:10.1103/PhysRevLett.45.963
- H. Bonet *et al.* [CONUS], Eur. Phys. J. C **82**, no.9, 813 (2022)

doi:10.1140/epjc/s10052-022-10722-1 [arXiv:2201.12257 [hep-ex]].

26. S. Navas *et al.* [Particle Data Group], Phys. Rev. D **110**, no.3, 030001 (2024) doi:10.1103/PhysRevD.110.030001

27. Phys. Rev. **73**, 416 (1948).

28. A. Cisneros, Astrophys. Space Sci. **10**, 87-92 (1971) doi:10.1007/BF00654607

29. C. Giunti, K. Kouzakov, Y. F. Li and A. Studenikin, doi:10.1146/annurev-nucl-102122-023242 [arXiv:2411.03122 [hep-ph]].

30. A. Aparici, K. Kim, A. Santamaria and J. Wudka, Phys. Rev. D **80**, 013010 (2009) doi:10.1103/PhysRevD.80.013010 [arXiv:0904.3244 [hep-ph]].

31. K. S. Babu, S. Jana and M. Lindner, JHEP **10**, 040 (2020) doi:10.1007/JHEP10(2020)040 [arXiv:2007.04291 [hep-ph]].

32. R. Plestid, Phys. Rev. D **104**, 075027 (2021) doi:10.1103/PhysRevD.104.075027 [arXiv:2010.04193 [hep-ph]].

33. V. Brdar, A. Greljo, J. Kopp and T. Opferkuch, JCAP **01**, 039 (2021) doi:10.1088/1475-7516/2021/01/039 [arXiv:2007.15563 [hep-ph]].

34. G. Magill, R. Plestid, M. Pospelov and Y. D. Tsai, Phys. Rev. D **98**, no.11, 115015 (2018) doi:10.1103/PhysRevD.98.115015 [arXiv:1803.03262 [hep-ph]].

35. A. A. Aguilar-Arevalo *et al.* [MiniBooNE], Phys. Rev. Lett. **102**, 101802 (2009) doi:10.1103/PhysRevLett.102.101802 [arXiv:0812.2243 [hep-ex]].

36. D. Akimov *et al.* [COHERENT], “Observation of Coherent Elastic Neutrino-Nucleus Scattering,” Science **357**, no.6356, 1123-1126 (2017) doi:10.1126/science.aa00990 [arXiv:1708.01294 [nucl-ex]].

37. M. Agostini *et al.* [Borexino], “Limiting neutrino magnetic moments with Borexino Phase-II solar neutrino data,” Phys. Rev. D **96**, no.9, 091103 (2017) doi:10.1103/PhysRevD.96.091103 [arXiv:1707.09355 [hep-ex]].

38. M. Deniz *et al.* [TEXONO], “Measurement of Nu(e)-bar -Electron Scattering Cross-Section with a CsI(Tl) Scintillating Crystal Array at the Kuo-Sheng Nuclear Power Reactor,” Phys. Rev. D **81**, 072001 (2010) doi:10.1103/PhysRevD.81.072001 [arXiv:0911.1597 [hep-ex]].

39. E. Aprile *et al.* [XENON], Phys. Rev. Lett. **133**, no.19, 191002 (2024) doi:10.1103/PhysRevLett.133.191002 [arXiv:2408.02877 [nucl-ex]].

40. Z. Bo *et al.* [PandaX], Phys. Rev. Lett. **133**, no.19, 191001 (2024) doi:10.1103/PhysRevLett.133.191001 [arXiv:2407.10892 [hep-ex]].

41. J. Aalbers *et al.* [LZ], Phys. Rev. Lett. **131**, no.4, 041002 (2023) doi:10.1103/PhysRevLett.131.041002 [arXiv:2207.03764 [hep-ex]].

42. G. G. Raffelt, “Limits on neutrino electromagnetic properties: An update,” Phys. Rept. **320**, 319–327 (1999). doi:10.1016/S0370-1573(99)00074-5

43. B. D. Fields, K. A. Olive, T.-H. Yeh and C. Young, “Big-Bang Nucleosynthesis after Planck,” JCAP **03**, 010 (2020) doi:10.1088/1475-7516/2020/03/010 [arXiv:1912.01132 [astro-ph.CO]].

44. N. Aghanim *et al.* [Planck], “Planck 2018 results. VI. Cosmological parameters,” Astron. Astrophys. **641**, A6 (2020) doi:10.1051/0004-6361/201833910 [arXiv:1807.06209 [astro-ph.CO]].

45. W. J. Marciano and A. I. Sanda, Phys. Lett. B **67**, 303-305 (1977) doi:10.1016/0370-2693(77)90377-X

46. P. B. Pal and L. Wolfenstein, Phys. Rev. D **25**, 766 (1982) doi:10.1103/PhysRevD.25.766

47. R. E. Shrock, Nucl. Phys. B **206**, 359-379 (1982) doi:10.1016/0550-3213(82)90273-5

48. C. Giunti, K. A. Kouzakov, Y. F. Li, A. V. Lokhov, A. I. Studenikin and S. Zhou, Annalen Phys. **528**, 198-215 (2016) doi:10.1002/andp.201500211 [arXiv:1506.05387 [hep-

ph]].

49. E. J. Chun, S. Mandal and R. Padhan, Phys. Rev. D **109**, no.11, 115002 (2024) doi:10.1103/PhysRevD.109.115002 [arXiv:2401.05174 [hep-ph]].
50. E. Bertuzzo and M. Frigerio, SciPost Phys. **18**, no.4, 140 (2025) doi:10.21468/SciPostPhys.18.4.140 [arXiv:2412.10101 [hep-ph]].
51. R. Beltrán, P. D. Bolton, F. F. Deppisch, C. Hati and M. Hirsch, JHEP **07**, 153 (2024) doi:10.1007/JHEP07(2024)153 [arXiv:2405.08877 [hep-ph]].
52. A. Ismail, S. Jana and R. M. Abraham, Phys. Rev. D **105**, no.5, 055008 (2022) doi:10.1103/PhysRevD.105.055008 [arXiv:2109.05032 [hep-ph]].
53. A. Ali, Phys. Rev. D **10**, 2801 (1974) doi:10.1103/PhysRevD.10.2801
54. Y. Zhang, M. Song, R. Ding and L. Chen, Phys. Lett. B **829**, 137116 (2022) doi:10.1016/j.physletb.2022.137116 [arXiv:2204.07802 [hep-ph]].
55. P. Vogel and J. Engel, Phys. Rev. D **39**, 3378 (1989) doi:10.1103/PhysRevD.39.3378
56. O. G. Miranda, G. Sanchez Garcia and O. Sanders, Adv. High Energy Phys. **2019**, 3902819 (2019) [erratum: Adv. High Energy Phys. **2022**, 9874517 (2022)] doi:10.1155/2019/3902819 [arXiv:1902.09036 [hep-ph]].
57. G. G. Raffelt, 1996, ISBN 978-0-226-70272-8
58. A. Ayala, J. C. D'Olivo and M. Torres, Phys. Rev. D **59**, 111901 (1999) doi:10.1103/PhysRevD.59.111901 [arXiv:hep-ph/9804230 [hep-ph]].
59. D. Z. Freedman, Phys. Rev. D **9**, 1389-1392 (1974) doi:10.1103/PhysRevD.9.1389
60. K. Scholberg, Phys. Rev. D **73**, 033005 (2006) doi:10.1103/PhysRevD.73.033005 [arXiv:hep-ex/0511042 [hep-ex]].
61. V. A. Bednyakov and D. V. Naumov, Phys. Rev. D **98**, no.5, 053004 (2018) doi:10.1103/PhysRevD.98.053004 [arXiv:1806.08768 [hep-ph]].
62. V. A. Bednyakov, D. V. Naumov and I. V. Titkova, Phys. Atom. Nucl. **84**, no.3, 314-327 (2021) doi:10.1134/S1063778821030066
63. A. A. Aguilar-Arevalo *et al.* [MiniBooNE], Phys. Rev. D **82**, 092005 (2010) doi:10.1103/PhysRevD.82.092005 [arXiv:1007.4730 [hep-ex]].
64. H. Duyang, B. Guo, S. R. Mishra and R. Petti, Eur. Phys. J. Plus **139**, no.11, 1014 (2024) doi:10.1140/epjp/s13360-024-05783-y [arXiv:1809.08752 [hep-ph]].
65. G. Radel and R. Beyer, Mod. Phys. Lett. A **8**, 1067-1088 (1993) doi:10.1142/S0217732393002567
66. O. Tomalak and R. J. Hill, Phys. Rev. D **101**, no.3, 033006 (2020) doi:10.1103/PhysRevD.101.033006 [arXiv:1907.03379 [hep-ph]].
67. C. F. Perdrisat, V. Punjabi and M. Vanderhaeghen, Prog. Part. Nucl. Phys. **59**, 694-764 (2007) doi:10.1016/j.ppnp.2007.05.001 [arXiv:hep-ph/0612014 [hep-ph]].
68. D. H. Beck and B. R. Holstein, Int. J. Mod. Phys. E **10**, 1-41 (2001) doi:10.1142/S0218301301000381 [arXiv:hep-ph/0102053 [hep-ph]].
69. R. H. Helm, Phys. Rev. **104**, 1466-1475 (1956) doi:10.1103/PhysRev.104.1466
70. J. Piekarewicz, A. R. Linero, P. Giuliani and E. Chicken, Phys. Rev. C **94**, no.3, 034316 (2016) doi:10.1103/PhysRevC.94.034316 [arXiv:1604.07799 [nucl-th]].
71. S. Klein and J. Nystrand, Phys. Rev. C **60**, 014903 (1999) doi:10.1103/PhysRevC.60.014903 [arXiv:hep-ph/9902259 [hep-ph]].
72. G. Duda, A. Kemper and P. Gondolo, JCAP **04**, 012 (2007) doi:10.1088/1475-7516/2007/04/012 [arXiv:hep-ph/0608035 [hep-ph]].
73. R. D. Woods and D. S. Saxon, Phys. Rev. **95**, 577-578 (1954) doi:10.1103/PhysRev.95.577
74. Y. F. Li and S. y. Xia, Phys. Rev. D **106**, no.9, 095022 (2022) doi:10.1103/PhysRevD.106.095022 [arXiv:2203.16525 [hep-ph]].
75. J. A. Formaggio and G. P. Zeller, Rev. Mod. Phys. **84**, 1307-1341 (2012)

doi:10.1103/RevModPhys.84.1307 [arXiv:1305.7513 [hep-ex]].

76. C. Athanassopoulos *et al.* [LSND], Phys. Rev. Lett. **77**, 3082-3085 (1996) doi:10.1103/PhysRevLett.77.3082 [arXiv:nucl-ex/9605003 [nucl-ex]].

77. A. A. Aguilar-Arevalo *et al.* [MiniBooNE], Phys. Rev. Lett. **121**, no.22, 221801 (2018) doi:10.1103/PhysRevLett.121.221801 [arXiv:1805.12028 [hep-ex]].

78. C. T. Kullenberg *et al.* [NOMAD], Phys. Lett. B **706**, 268-275 (2012) doi:10.1016/j.physletb.2011.11.049 [arXiv:1111.3713 [hep-ex]].

79. M. Anelli *et al.* [SHiP], [arXiv:1504.04956 [physics.ins-det]].

80. R. Acciarri *et al.* [MicroBooNE, LAr1-ND and ICARUS-WA104], [arXiv:1503.01520 [physics.ins-det]].

81. A. G. Beda, V. B. Brudanin, V. G. Egorov, D. V. Medvedev, V. S. Pogosov, M. V. Shirchenko and A. S. Starostin, Adv. High Energy Phys. **2012**, 350150 (2012) doi:10.1155/2012/350150

82. H. T. Wong *et al.* [TEXONO], Phys. Rev. D **75**, 012001 (2007) doi:10.1103/PhysRevD.75.012001 [arXiv:hep-ex/0605006 [hep-ex]].

83. M. Deniz *et al.* [TEXONO], Phys. Rev. D **81**, 072001 (2010) doi:10.1103/PhysRevD.81.072001 [arXiv:0911.1597 [hep-ex]].

84. A. G. Beda, V. B. Brudanin, V. G. Egorov, D. V. Medvedev, V. S. Pogosov, E. A. Shevchik, M. V. Shirchenko, A. S. Starostin and I. V. Zhitnikov, Phys. Part. Nucl. Lett. **10**, 139-143 (2013) doi:10.1134/S1547477113020027

85. E. Aprile *et al.* [XENON], Phys. Rev. D **102**, no.7, 072004 (2020) doi:10.1103/PhysRevD.102.072004 [arXiv:2006.09721 [hep-ex]].

86. D. Akimov *et al.* [COHERENT], Phys. Rev. Lett. **126**, no.1, 012002 (2021) doi:10.1103/PhysRevLett.126.012002 [arXiv:2003.10630 [nucl-ex]].

87. A. Aguilar-Arevalo *et al.* [CONNIE], JHEP **05**, 017 (2022) doi:10.1007/JHEP05(2022)017 [arXiv:2110.13033 [hep-ex]].

88. H. Bonet *et al.* [CONUS], Phys. Rev. Lett. **126**, no.4, 041804 (2021) doi:10.1103/PhysRevLett.126.041804 [arXiv:2011.00210 [hep-ex]].

89. D. Barducci, W. Liu, A. Titov, Z. S. Wang and Y. Zhang, Phys. Rev. D **108**, no.11, 115009 (2023) doi:10.1103/PhysRevD.108.115009 [arXiv:2308.16608 [hep-ph]].

90. N. M. Kroll and W. Wada, Phys. Rev. **98**, 1355-1359 (1955) doi:10.1103/PhysRev.98.1355

91. K. O. Mikaelian and J. Smith, Phys. Rev. D **5**, 1763-1773 (1972) doi:10.1103/PhysRevD.5.1763

92. L. G. Landsberg, Phys. Rept. **128**, 301-376 (1985) doi:10.1016/0370-1573(85)90129-2

93. B. Dutta, D. Goswami, A. Karthikeyan and K. J. Kelly, JHEP **05**, 240 (2025) doi:10.1007/JHEP05(2025)240 [arXiv:2501.09840 [hep-ph]].

94. S. Kanemura, T. Moroi and T. Tanabe, Phys. Lett. B **751**, 25-28 (2015) doi:10.1016/j.physletb.2015.10.002 [arXiv:1507.02809 [hep-ph]].

95. P. Giffin, S. Gori, Y. D. Tsai and D. Tuckler, JHEP **04**, 046 (2023) doi:10.1007/JHEP04(2023)046 [arXiv:2206.13745 [hep-ph]].

96. M. Ablikim *et al.* [BESIII], Phys. Rev. D **83**, 112005 (2011) doi:10.1103/PhysRevD.83.112005 [arXiv:1103.5564 [hep-ex]].

97. T. Abe *et al.* [Belle-II], [arXiv:1011.0352 [physics.ins-det]].

98. R. Tiwary, [arXiv:2404.01957 [hep-ex]].

99. H. Abreu *et al.* [FASER], JINST **19**, no.05, P05066 (2024) doi:10.1088/1748-0221/19/05/P05066 [arXiv:2207.11427 [physics.ins-det]].

100. S. Cerci, D. Sunar Cerci, D. Lazic, G. Landsberg, F. Cerutti, M. Sabate-Gilarte, M. G. Albrow, J. Berryhill, D. R. Green and J. Hirschauer, *et al.* JHEP **06**, 110 (2022) doi:10.1007/JHEP06(2022)110 [arXiv:2201.00019 [hep-ex]].

101. E. Cortina Gil *et al.* [NA62], JINST **12**, no.05, P05025 (2017) doi:10.1088/1748-0221/12/05/P05025 [arXiv:1703.08501 [physics.ins-det]].
102. E. Cortina Gil *et al.* [NA62], Phys. Lett. B **850**, 138513 (2024) doi:10.1016/j.physletb.2024.138513 [arXiv:2311.01837 [hep-ex]].
103. T. Abe *et al.* [Belle II Collaboration], “Belle II Technical Design Report,” KEK Report 2010-1 (2010).
104. R. Aaij *et al.* [LHCb Collaboration], “LHCb Detector performance,” Int. J. Mod. Phys. A **30**, 1530022 (2015); see also VELO performance updates in Run 2 documentation.
105. C. Abellán Beteta, A. Alfonso Albero, Y. Amhis, S. Barsuk, C. Beigbeder-Beau, I. Belyaev, R. Bonnefoy, D. Breton, O. Callot and M. Calvo Gomez, *et al.* [arXiv:2008.11556 [physics.ins-det]].
106. D. Buskulic *et al.* [ALEPH], Phys. Lett. B **313**, 520-534 (1993) doi:10.1016/0370-2693(93)90027-F
107. G. Abbiendi *et al.* [OPAL], Eur. Phys. J. C **18**, 253-272 (2000) doi:10.1007/s100520000522 [arXiv:hep-ex/0005002 [hep-ex]].
108. M. Aaboud *et al.* [ATLAS], Phys. Rev. D **96**, no.11, 112004 (2017) doi:10.1103/PhysRevD.96.112004 [arXiv:1706.03948 [hep-ex]].
109. A. M. Sirunyan *et al.* [CMS], JHEP **10**, 073 (2017) doi:10.1007/JHEP10(2017)073 [arXiv:1706.03794 [hep-ex]].
110. C. A. Argüelles, N. Foppiani and M. Hostert, Phys. Rev. D **105**, no.9, 095006 (2022) doi:10.1103/PhysRevD.105.095006 [arXiv:2109.03831 [hep-ph]].
111. FASER Collaboration, “FASER’s Physics Reach for Long-Lived Particles,” Phys. Rev. D **99**, no.9, 095011 (2019) [arXiv:1811.12522 [hep-ph]].
112. G. Aad *et al.* [ATLAS], Phys. Rev. D **108** (2023) no.3, 032016 doi:10.1103/PhysRevD.108.032016 [arXiv:2209.01029 [hep-ex]].
113. A. M. Sirunyan *et al.* [CMS], Phys. Rev. D **100** (2019) no.11, 112003 doi:10.1103/PhysRevD.100.112003 [arXiv:1909.06166 [hep-ex]].
114. T. Schwetz, A. Zhou and J. Y. Zhu, JHEP **21** (2020), 200 doi:10.1007/JHEP07(2021)200 [arXiv:2105.09699 [hep-ph]].
115. D. Barducci, E. Bertuzzo, M. Taoso, C. A. Ternes and C. Toni, JHEP **10**, 016 (2024) doi:10.1007/JHEP10(2024)016 [arXiv:2406.17599 [hep-ph]].
116. K. Abe *et al.* [T2K], Phys. Rev. D **100**, no.5, 052006 (2019) doi:10.1103/PhysRevD.100.052006 [arXiv:1902.07598 [hep-ex]].
117. R. Acciarri *et al.* [DUNE], [arXiv:1512.06148 [physics.ins-det]].
118. C. Ahdida *et al.* [SHiP], JHEP **04** (2019), 077 doi:10.1007/JHEP04(2019)077 [arXiv:1811.00930 [hep-ph]].
119. I. M. Shoemaker and J. Wyenberg, Phys. Rev. D **99**, no.7, 075010 (2019) doi:10.1103/PhysRevD.99.075010 [arXiv:1811.12435 [hep-ph]].
120. E. Cortina Gil *et al.* [NA62], Phys. Lett. B **807**, 135599 (2020) doi:10.1016/j.physletb.2020.135599 [arXiv:2005.09575 [hep-ex]].
121. M. U. Ashraf *et al.* [HIKE], [arXiv:2311.08231 [hep-ex]].
122. G. Bellini *et al.* [Borexino], Phys. Lett. B **696**, 191-196 (2011) doi:10.1016/j.physletb.2010.12.030 [arXiv:1010.0029 [hep-ex]].
123. A. Drukier and L. Stodolsky, Phys. Rev. D **30**, 2295 (1984) doi:10.1103/PhysRevD.30.2295
124. J. Barranco, O. G. Miranda and T. I. Rashba, JHEP **12**, 021 (2005) doi:10.1088/1126-6708/2005/12/021 [arXiv:hep-ph/0508299 [hep-ph]].
125. K. Patton, J. Engel, G. C. McLaughlin and N. Schunck, Phys. Rev. C **86**, 024612

(2012) doi:10.1103/PhysRevC.86.024612 [arXiv:1207.0693 [nucl-th]].

126. M. Cadeddu, F. Dordei, C. Giunti, Y. F. Li, E. Picciano and Y. Y. Zhang, Phys. Rev. D **102**, no.1, 015030 (2020) doi:10.1103/PhysRevD.102.015030 [arXiv:2005.01645 [hep-ph]].

127. A. Dasgupta, S. K. Kang and J. E. Kim, JHEP **11**, 120 (2021) doi:10.1007/JHEP11(2021)120 [arXiv:2108.12998 [hep-ph]].

128. D. Akimov *et al.* [COHERENT], Science **357**, no.6356, 1123-1126 (2017) doi:10.1126/science.aa00990 [arXiv:1708.01294 [nucl-ex]].

129. D. Akimov *et al.* [COHERENT], doi:10.5281/zenodo.1228631 [arXiv:1804.09459 [nucl-ex]].

130. R. Harnik, J. Kopp and P. A. N. Machado, JCAP **07**, 026 (2012) doi:10.1088/1475-7516/2012/07/026 [arXiv:1202.6073 [hep-ph]].

131. A. B. Balantekin and N. Vassh, Phys. Rev. D **89**, no.7, 073013 (2014) doi:10.1103/PhysRevD.89.073013 [arXiv:1312.6858 [hep-ph]].

132. L. B. Auerbach *et al.* [LSND], Phys. Rev. D **63**, 112001 (2001) doi:10.1103/PhysRevD.63.112001 [arXiv:hep-ex/0101039 [hep-ex]].

133. D. Geiregat *et al.* [CHARM-II], Phys. Lett. B **232**, 539 (1989) doi:10.1016/0370-2693(89)90457-7

134. J. Altegoer *et al.* [NOMAD], Nucl. Instrum. Meth. A **404**, 96-128 (1998) doi:10.1016/S0168-9002(97)01079-6

135. R. Schwienhorst *et al.* [DONUT], Phys. Lett. B **513**, 23-29 (2001) doi:10.1016/S0370-2693(01)00746-8 [arXiv:hep-ex/0102026 [hep-ex]].

136. K. Abe *et al.* [T2K], [arXiv:1901.03750 [physics.ins-det]].

137. M. G. Aartsen *et al.* [IceCube], Astrophys. J. **833**, no.1, 3 (2016) doi:10.3847/0004-637X/833/1/3 [arXiv:1607.08006 [astro-ph.HE]].

138. K. Abe *et al.* [Super-Kamiokande], Phys. Rev. D **94**, no.5, 052010 (2016) doi:10.1103/PhysRevD.94.052010 [arXiv:1606.07538 [hep-ex]].

139. N. Ackermann *et al.* [CONUS+], Eur. Phys. J. C **84**, no.12, 1265 (2024) [erratum: Eur. Phys. J. C **85**, no.1, 19 (2025)] doi:10.1140/epjc/s10052-024-13551-6 [arXiv:2407.11912 [hep-ex]].

140. D. Aristizabal Sierra, V. De Romeri and D. K. Papoulias, JHEP **09**, 076 (2022) doi:10.1007/JHEP09(2022)076 [arXiv:2203.02414 [hep-ph]].

141. V. De Romeri, D. K. Papoulias and G. Sanchez Garcia, Phys. Rev. D **111**, no.7, 7 (2025) doi:10.1103/PhysRevD.111.075025 [arXiv:2501.17843 [hep-ph]].

142. S. N. Gninenco, Phys. Rev. D **83**, 015015 (2011) doi:10.1103/PhysRevD.83.015015 [arXiv:1009.5536 [hep-ph]].

143. M. Masip, P. Masjuan and D. Meloni, JHEP **01**, 106 (2013) doi:10.1007/JHEP01(2013)106 [arXiv:1210.1519 [hep-ph]].

144. S. N. Gninenco, Phys. Rev. Lett. **103**, 241802 (2009) doi:10.1103/PhysRevLett.103.241802 [arXiv:0902.3802 [hep-ph]].

145. S. Vergani, N. W. Kamp, A. Diaz, C. A. Argüelles, J. M. Conrad, M. H. Shaevitz and M. A. Uchida, Phys. Rev. D **104**, no.9, 095005 (2021) doi:10.1103/PhysRevD.104.095005 [arXiv:2105.06470 [hep-ph]].

146. P. Coloma, P. A. N. Machado, I. Martinez-Soler and I. M. Shoemaker, Phys. Rev. Lett. **119**, no.20, 201804 (2017) doi:10.1103/PhysRevLett.119.201804 [arXiv:1707.08573 [hep-ph]].

147. S. N. Gninenco and N. V. Krasnikov, Phys. Lett. B **450**, 165-172 (1999) doi:10.1016/S0370-2693(99)00130-6 [arXiv:hep-ph/9808370 [hep-ph]].

148. S. N. Gninenco and N. V. Krasnikov, Phys. Lett. B **427**, 307-313 (1998) doi:10.1016/S0370-2693(98)00358-X [arXiv:hep-ph/9802375 [hep-ph]].

149. L. Zazueta *et al.* [MINERvA], Phys. Rev. D **107**, no.1, 012001 (2023) doi:10.1103/PhysRevD.107.012001 [arXiv:2209.05540 [hep-ex]].

150. M. S. Liu, N. Kamp and C. A. Argüelles, Phys. Rev. D **112**, no.3, 035012 (2025) doi:10.1103/5738-hj4s [arXiv:2412.15051 [hep-ph]].

151. M. Agostini *et al.* [BOREXINO], Nature **562**, no.7728, 505-510 (2018) doi:10.1038/s41586-018-0624-y

152. R. Agnese *et al.* [SuperCDMS], Phys. Rev. D **97**, no.2, 022002 (2018) doi:10.1103/PhysRevD.97.022002 [arXiv:1707.01632 [astro-ph.CO]].

153. P. D. Bolton, F. F. Deppisch, K. Fridell, J. Harz, C. Hati and S. Kulkarni, Phys. Rev. D **106**, no.3, 035036 (2022) doi:10.1103/PhysRevD.106.035036 [arXiv:2110.02233 [hep-ph]].

154. C. A. Ternes and M. Tórtola, Nucl. Phys. B **1019**, 117107 (2025) doi:10.1016/j.nuclphysb.2025.117107 [arXiv:2505.02633 [hep-ph]].

155. D. Akimov *et al.* [COHERENT], [arXiv:1509.08702 [physics.ins-det]].

156. D. Akimov *et al.* [COHERENT], doi:10.5281/zenodo.3903810 [arXiv:2006.12659 [nucl-ex]].

157. V. De Romeri, D. K. Papoulias, G. Sanchez Garcia, C. A. Ternes and M. Tórtola, JCAP **05**, 080 (2025) doi:10.1088/1475-7516/2025/05/080 [arXiv:2412.14991 [hep-ph]].

158. N. Sabti, A. Magalich and A. Filimonova, JCAP **11**, 056 (2020) doi:10.1088/1475-7516/2020/11/056 [arXiv:2006.07387 [hep-ph]].

159. R. J. Cooke, M. Pettini and C. C. Steidel, Astrophys. J. **855**, no.2, 102 (2018) doi:10.3847/1538-4357/aaab53 [arXiv:1710.11129 [astro-ph.CO]].

160. K. Bleau, J. Bramante and C. Cappiello, JCAP **01**, 021 (2024) doi:10.1088/1475-7516/2024/01/021 [arXiv:2309.06482 [hep-ph]].

161. Particle Data Group, S. Navas *et al.*, “Big-Bang Nucleosynthesis,” *Prog. Theor. Exp. Phys.* **2024**, 083C01 (2024), doi:10.1093/ptep/ptae067. Available at: <https://pdg.lbl.gov/2024/reviews/rpp2024-rev-bbang-nucleosynthesis.pdf>

162. M. Escudero Abenza, JCAP **05**, 048 (2020) doi:10.1088/1475-7516/2020/05/048 [arXiv:2001.04466 [hep-ph]].

163. E. W. Kolb and M. S. Turner, *The Early Universe*, (Addison–Wesley, Redwood City, USA, 1990).

164. G. Mangano, G. Miele, S. Pastor, T. Pinto, O. Pisanti and P. D. Serpico, “Relic neutrino decoupling including flavour oscillations,” Nucl. Phys. B **729**, 221–234 (2005), doi:10.1016/j.nuclphysb.2005.09.041, [arXiv:hep-ph/0506164].

165. P. F. de Salas and S. Pastor, “Relic neutrino decoupling with flavour oscillations revisited,” JCAP **07**, 051 (2016), doi:10.1088/1475-7516/2016/07/051, [arXiv:1606.06986 [hep-ph]].

166. J. M. Lattimer and J. Cooperstein, Phys. Rev. Lett. **61**, 23-26 (1988) [erratum: Phys. Rev. Lett. **61**, 2633 (1988)] doi:10.1103/PhysRevLett.61.23

167. A. Caputo, G. Raffelt and E. Vitagliano, Phys. Rev. D **105**, no.3, 035022 (2022) doi:10.1103/PhysRevD.105.035022 [arXiv:2109.03244 [hep-ph]].

168. G. Chauhan, S. Horiuchi, P. Huber and I. M. Shoemaker, Phys. Rev. D **110**, no.1, 015007 (2024) doi:10.1103/PhysRevD.110.015007 [arXiv:2402.01624 [hep-ph]].

169. K. Hirata *et al.* [Kamiokande-II], Phys. Rev. Lett. **58**, 1490-1493 (1987) doi:10.1103/PhysRevLett.58.1490

170. R. M. Bionta, G. Blewitt, C. B. Bratton, D. Casper, A. Ciocio, R. Claus, B. Cortez, M. Crouch, S. T. Dye and S. Errede, *et al.* Phys. Rev. Lett. **58**, 1494 (1987) doi:10.1103/PhysRevLett.58.1494

171. E. N. Alekseev, L. N. Alekseeva, V. I. Volchenko and I. V. Krivosheina, JETP Lett. **45**, 589-592 (1987)

172. M. Kawasaki, K. Kohri and T. Moroi, “Big-Bang nucleosynthesis and hadronic decay of long-lived massive particles,” *Phys. Rev. D* **71**, 083502 (2005), doi:10.1103/PhysRevD.71.083502, [arXiv:astro-ph/0408426].
173. M. Kawasaki, K. Kohri and T. Moroi, “Revised Big-Bang nucleosynthesis with long-lived decaying particles,” *Phys. Rev. D* **78**, 065011 (2008), doi:10.1103/PhysRevD.78.065011, [arXiv:0804.3745 [hep-ph]].
174. J. Baur, N. Palanque-Delabrouille, C. Yèche, C. Magneville, and M. Viel, “Lyman- α Forests cool Warm Dark Matter,” *JCAP* **08**, 012 (2016) doi:10.1088/1475-7516/2016/08/012 [arXiv:1512.01981 [astro-ph.CO]].
175. M. Escudero and S. J. Witte, *Eur. Phys. J. C* **80**, no.4, 294 (2020) doi:10.1140/epjc/s10052-020-7854-5 [arXiv:1909.04044 [astro-ph.CO]].
176. J. H. Chang, R. Essig and S. D. McDermott, *JHEP* **01**, 107 (2017) doi:10.1007/JHEP01(2017)107 [arXiv:1611.03864 [hep-ph]].
177. P. Carenza and G. Lucente, *Phys. Rev. D* **103**, no.12, 123024 (2021) doi:10.1103/PhysRevD.103.123024 [arXiv:2104.09524 [hep-ph]].
178. G. Kallen, Elementary particle physics. Addison-Wesley series in advanced physics. Addison-Wesley Pub. Co., 1964.
179. K. Bondarenko, A. Boyarsky, D. Gorbunov and O. Ruchayskiy, *JHEP* **11**, 032 (2018) doi:10.1007/JHEP11(2018)032 [arXiv:1805.08567 [hep-ph]].